NONLINEAR ANALYSIS OF THE GROUND-BASED MAGNETOMETER NETWORK

By

Joseph Henry DiTommaso

RECOMMENDED:

Dr. Renate A. Wackerbauer

Dr. Hui Zhang

Dr. David Newman, Advisory Committee Chair

Dr. Renate A. Wackerbauer, Chair, Department of Physics

APPROVED:

Dr. Paul W. Layer
Dean, College of Natural Science and Mathematics

Dr. John C. Eichelberger
Dean of the Graduate School

12 August 2015
Date

NONLINEAR ANALYSIS OF THE GROUND-BASED MAGNETOMETER NETWORK

A

THESIS

Presented to the Faculty

of the University of Alaska Fairbanks

in Partial Fulfillment of the Requirements

for the Degree of

MASTER OF SCIENCE

By

Joseph Henry DiTommaso, B.S.

Fairbanks, AK

August 2015

Abstract

When the first magnetometer was created by Frederick Gauss in 1833, scientists gained a powerful tool for studying the structure, dynamics, and strength of the Earth's magnetic field: the magnetosphere. Since Gauss' time, the world's scientific community has established ground-based magnetometer stations around the globe in an effort to study local and global perturbations and patterns of the Earth's magnetic field. The main focus of this network has been monitoring the magnetic flux and impact from the Sun's constant outflow of radiation and particles known as the solar wind, as well as its more violent eruptive events. There has been little work, by comparison, into the signals and correlations within the network itself. Since the Earth's field can roughly be mapped to a dipole and disturbances often have a large scale structure, one can surmise there should be some correlation between stations based on their relative positions to one another. What that correlation is or represents is not clear. To investigate this possible correlation and its nature, a set of nonlinear analytic methods were conducted on magnetic data collected from stations scattered across North America over an 18 year period. The analysis was focused on searching for spatial and temporal correlations of nonperiodic signals in the magnetometer network. The findings from that analysis suggest there exist nonlocal correlations between stations that are dependent on position, which could be useful in the development of a space weather risk assessment.

Dedication

I would like to dedicate this thesis to my family, friends, and mentors who have supported me on this long journey.

To my family, thank you for raising me to be the man I am today with your love and guidance. I would like to especially thank my mother, for her inspiration to follow my dreams and fly high. I love you all!

To my friends, thank you for sharing in my adventures and giving my life the excitement and flavor it so richly enjoys. To my best friend, Alan, thank you for always putting a smile on my face and believing in me.

To my mentors, thank you for setting me on the path to science and always helping me find my way. Genene and Bill, thank you for bringing me into the world of space weather!

To Kaz, thank you for everything. You are everything I could want in a companion to walk beside me on this path. I will love and cherish you always.

Table of Contents

Page

List of Figures

Page

List of Tables

Acknowledgments

This thesis would not have been possibly without the support, guidance, patience, and expertise of my Master's committee. Thank you Dr. Renate Wackerbauer for your friendliness, great advice, and wonderful sense of humor. Thank you Dr. Hu Zhang for your lessons both in and out of the class on space physics, as well as your professionalism.

I would also like to recognize the other students in the Complex Dynamical Group for their aide in both my research and writing. I would especially like to thank Douglas Ogata for taking me under his wing as a researcher and programmer. I would like to confer the title of 'honorary' second author to you for this thesis for your immeasurable help.

Finally, though this journey was a long and tenuous one, you never faltered in your quest to guide and motivate me through this research. You have been more than a professional academic mentor to me, you have helped me in so much in my personal life as well. So thank you with all of my heart to my advisor, Dr. David Newman, for your brilliance, patience, passion, and for taking this journey with me.

Chapter 1 Introduction

1.1 Space Weather

With each passing year, society is becoming more and more dependent on technology that is susceptible to the impacts of space weather. The study of space weather focuses on understanding, predicting, and mitigating the effects of solar storms on both society and technology. Space weather research focuses on the Sun-Earth system, the complicated interactions between the magnetospheres of both our planet and the Sun, the Earth's ionosphere and atmosphere, and the Sun's solar wind and energetic eruptions. The solar wind, an ever-present and varying outflow of charged particles and radiation, is constantly buffering and enveloping the Earth, as well as all other bodies in the solar system. Solar flares, coronal mass ejections, and other violent eruptions of plasma and radiation constitute the majority of severe space weather events. Overall, our understanding of how mankind and its technology are susceptible and vulnerable to space weather events is ever evolving in response to the need to protect against those dangers.

As an ensemble science that combines multiple disciplines and technologies to focus on the Sun-Earth interaction, research in space weather can be divided into three main areas. Solar, interplanetary, and heliospheric researchers investigate "the processes by which energy in the form of magnetic fields and particles are produced by the Sun and/or accelerated in interplanetary space and on the mechanisms by which these fields and particles are transported to the Earth through the inner heliosphere" [NSF, 2015]. Magnetospheric studies focus on how plasma interacts, enters, is stored, and transported within the various regions of the magnetosphere [Kivelson and Russell, 1995]. Aeronomists and ionospheric physicists study the upper atmospheric and ionospheric interactions with the precipitating high energy particles and electromagnetic waves [Kivelson and Russell, 1995]. Other various disciplines of physics and engineering focus on the technological infrastructure while prediction specialists work with modelers to create models for forecasting space weather events and impacts. Large industries with technological vulnerabilities to space weather, such as aviation, the power grid, communication, oil and gas utilities, and GPS are joined by smaller interest groups such as pigeon racing and space tourism to create a private/public sector coalition of interested parties [Lanzerotti, 2001]. These industries help drive the forecasting and technological advancements in the science, while academic research drives the fundamental understanding. Together this space

weather community works to "study and teach space weather science as a single, unified discipline, a strategy popularly dubbed the Sun-to-mud approach"[Simpson, 2004].

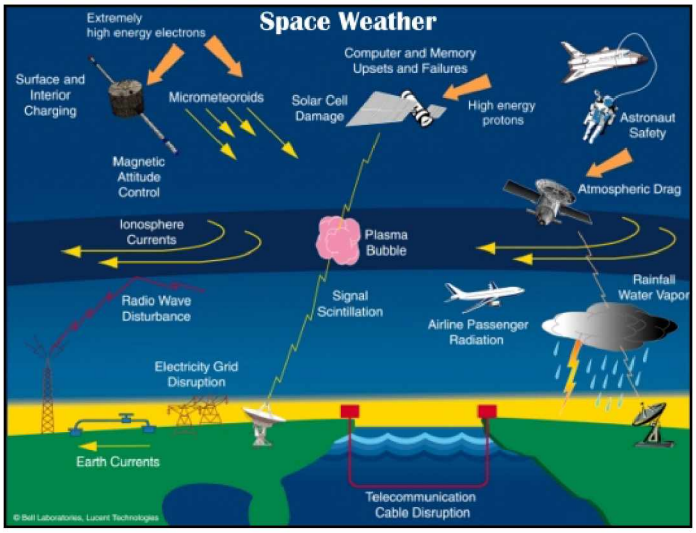

Figure 1.1: Space Weather Impacts [Lanzerotti, 2001]

Figure 1.1 depicts some of the known space weather impacts as described by Lanzerotti [2001]. Areas of concern for impacts of energetic events can be categorized into several main groups: satellites, power grids, human health, oil/gas/water pipelines, and aviation [Lanzerotti, 2001]. Satellites are the most vulnerable technology due to their positioning outside the Earth's atmosphere and sometimes even the magnetosphere. Surface charging, high energetic particle impacts, radio spikes, and other effects can directly damage the hardware on the satellites themselves. Changes in the ionosphere, especially the total electron count (TEC), can disrupt satellite signal (especially for GPS) causing scintillation and range errors. Smaller effects, such as the expansion of the Earth's exosphere due to heating which can be "sufficient to raise the top of the atmosphere by several hundred km during solar maximum" [Lanzerotti, 2001], affecting the longevity of a satellite by increasing orbital drag. Impacts on human health initially were concerned with only hazards for astronauts but has expanded to high altitude and high latitude frequent fliers as "the crew and frequent fliers are prone to unhealthy effects of radiation" [Pirjola et al., 2005]. Other aviation impacts come from navigation control due to GPS and communication, especially for cross-polar flights where out of line of sight for satellite communication pilots are required to use high frequency (HF) communications that bounces signals off the ionosphere. If the ionospheric conditions change, the HF signal can get scrambled or lost, leaving a cockpit crew without any contact with

the ground [Pirjola et al., 2005]. Gummow and Eng [2002] and Boteler et al. [1998] demonstrated that geomagnetically induced currents (GIC) create problems associated with corrosion and failures in oil/gas/utility pipelines and telecommunication equipment, respectively, buried in the ground. Finally, the electrical underpinning of society, the power grid, is highly vulnerable to GICs that feed into the lines. This can cause anything from simple degradation due to ohmic heating to total collapse and destruction of transformers, as seen in Quebec in 1989. This event left millions without power for over 8 hours, resulting in a loss of over 20,000 Megawatts with total system collapse happening roughly 90 seconds after onset of issues [Fisher, 2003]. Concern over how an even larger event would impact the planet has led to modelling and investigation into the 1859 Carrington Event. This was the first observed flare connected to a terrestrial response and represents a 'worst case scenario' [Cliver, 2006]. The flare and subsequent geomagnetic storm were so strong that the telegraph systems of the day were able to run without the batteries connected for several hours and the subsequent aurora was observed as far south as Cuba [Lanzerotti, 2001]. What effect a Carrington level event would have on today's systems is a topic of great research and modelling in space weather [Cliver, 2006].

In such a vast and complicated area of interest, a number of significant challenges for data collection, modelling, theory, and prediction exist. First and foremost, in situ data collection of space weather events is currently handled by a collection of satellites. While the number of satellites studying the Sun have grown in years, there is no question that there is an incalculable amount of data missing to complete the picture. For studying the Earth's magnetosphere, in situ measurements are handled by satellites, ground-based magnetometers, as well as some rocket and balloon soundings (though these are relegated to specific studies compared to daily observation). Ionospheric and upper atmosphere readings have a vast array of remote sensing data collection, with only balloon and rocket launches occasionally gathering in situ measurements. Both spatial and temporal coverage are major concerns in the observation of the magnetosphere. Many satellites that orbit the Earth or Sun are either fixed to one position (i.e. geostationary) only giving data on that one spot or polar orbiting, giving measurements on a time interval of an hour to a day in some cases. In monitoring the Sun and energetic events heading toward the Earth, there are only a few satellites at the L1 Lagrange position such as the Advanced Composition Explorer (ACE). This position is roughly a tenth of the distance to the Sun from the Earth, at a point where both

the Sun's and Earth's gravity roughly counteract each other. This allows ACE and other platforms to remain at a stable position between the Earth and the Sun. These satellites act as the one main buoy in the way of solar events that give warning and data on the strength and composition of events as it heads to Earth [Space Studies Board et al., 2008].

Due to the size of the system that space weather research studies, there are still great challenges in data collection. The National Weather Services Space Weather Prediction Center (NWS SWPC) has been working tirelessly to host, maintain, analyze, model, and eventually utilize the observations for predictive and advisory actions. SWPC is the "nations official source of space weather alerts, watches, and warnings" [Fisher et al., 2009] and is the space weather arm of the NWS. The transition from many small groups collecting one particular array of data (for example the College magnetometer at the University of Alaska) to a network and database is still an ongoing process [Fisher et al., 2009]. NASA, ESA, USGS, numerous universities and other institutions are slowly sharing information around the world, so that research such as this project can be done and then disseminated across the scientific community. NASA missions, in particular, "supply substantial and critical space weather information... but do not provide situational awareness and forecasting services" [Space Studies Board et al., 2008]. This networking within the space weather field, mimicking the organization, growth and development of the meteorological community, has led to a fast growing interconnected community that is working to meet the burgeoning needs of a technologically advancing society [Fisher et al., 2009]. The work presented herein is aimed at better understanding the downstream interlinking of events and look for correlations that could help create a space weather risk metric.

1.2 Earth's Magnetosphere

In order to study space weather events and impacts, one must first understand the environment they occur in, the Earth's magnetosphere. The magnetosphere of the Earth is a semi-closed magnetic field thought to be driven by the dynamo effect of the Earth's rotating core. Figure 1.2 depicts a rough diagram of the shape and various regions of the magnetosphere. While being mostly a dipole in nature, it is not symmetric, being compressed by the solar wind on the day side and stretched on the night. The dayside compression brings the edge to only about 6 to 10 Earth radii. In contrast, the nightside magnetotail is stretched out in upwards of 1000 Earth radii [Kivelson and

Russell, 1995]. A bow shock is formed ahead of the magnetosphere, slowing the supersonic solar wind to subsonic speeds. The poles of the field are reversed compared to the geographic poles, where the southern magnetic pole is near the northern geographic pole. The field intersects with the ground, known as the foot of the line, leading to increased penetration in the higher latitudes by charged particles and radiation. Between the bow shock and the edge of the magnetosphere, the magnetopause, is the turbulent magnetosheath. There are 2 openings in the field lines, known as cusps, that allow magnetosheath plasma direct access to the ionosphere [Kivelson and Russell, 1995].

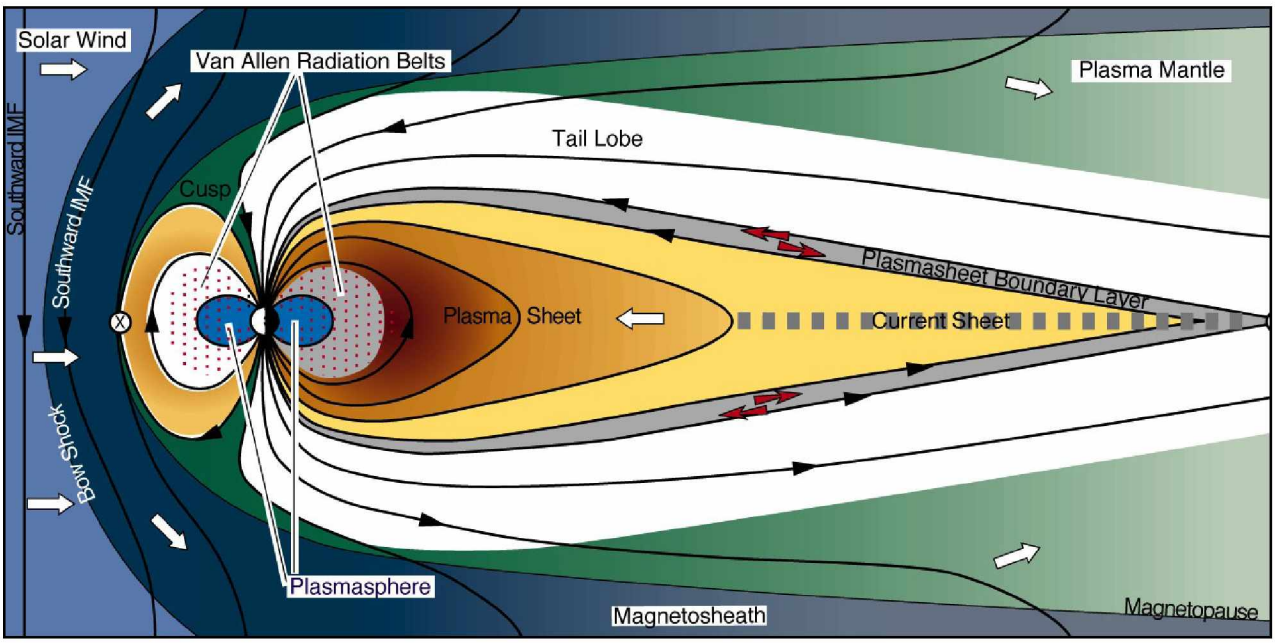

Figure 1.2: Regions of the Magnetosphere [Reiff, 1999]

Within the magnetosphere are several distinct regions that store a certain type of characteristic plasma. The plasma mantle consists of the region nearest the magnetopause, and consists of very cool, dense plasma. The tail lobe region consists of plasma with a similar temperature to the mantle but less dense, located in the extended magnetotail. The plasma/current sheet is a thin area of dense, hot plasma in center of the magnetotail. The most energetic and densest plasma is in the very center, falling off toward the boundary layer. The near Earth region of the magnetosphere consists of the relatively cool plasmasphere and the active Van Allen radiation belts. The radiation belts are a set of dynamic arcs of very hot plasma (on the order of MeV) that is very sensitive to substorm activity. The various regions act as sources and sinks of energetic electrons and pro-

tons, which can transport down into the atmosphere or remain locked within the magnetosphere [Kivelson and Russell, 1995]. Table 1.1 provides an estimation for the characteristic parameters of density, thermal energy, and the ratio of plasma pressure to magnetic pressure, plasma β. Transport between these regions is a highly studied area of interest, as there are numerous types of waves, particle motion, and most important for this paper, currents and fields.

Table 1.1: Typical Plasma and Magnetic Field Parameters in the Earth's Magnetosphere

Region	Density (cm^3)	Thermal Energy (eV)	Plasma β
Solar Wind	3-20	10	10
Magnetosheath	2-50	100	1-10
Plasma Mantle	0.01-1	100	0.001-0.1
Tail Lobe	0.01	100	0.001
Plasma Sheet Boundary Layer	0.1	1,000	0.01
Central Plasma Sheet	0.5	5,000	10
Plasmasphere	100	1 eV	Varies with r

Values taken from [Kivelson and Russell, 1995] and [Parks, 2004]

Critical to this research are the measurements of the induced fields on the Earth's surface which are what is measured by the instrumentation. As described in Kivelson and Russell [1995], there are numerous currents in the magnetosphere and ionosphere which can evolve over time as the magnetospheric environment changes under the influence of the solar wind and eruptive events. Due to the changes in these currents, magnetic and electric fields are induced in the atmosphere and ground [Kivelson and Russell, 1995]. These, in turn are measured by the instrumentation on the ground either by direct measurement of the field or by measurement of the induced current in the instrument by the evolving field. These geomagnetically induced currents, as mentioned before, are also responsible for damages to the power grid and utility lines in the ground.

With the understanding of the environment the research takes place in, the rest of the thesis is organized to introduce the physical data, the methods, and the results of analysis. The data set utilized and preparation methods for said data are discussed in Chapter 2. Chapter 3 describes what analysis methods were implemented and their purpose. The results of applying the analysis methods to the data, including noticeable trends, possible interpretations of observed characteristics, and difficulties present in the analysis, are covered in Chapter 4. Chapter 5 summarizes the findings of the research as well as presenting suggested future work.

Chapter 2 Data Set & Data Preparation

As the most impactive events of space weather pertain to the induced currents at the ground, the magnetic fields that create said currents need to be measured. To do so, a magnetometer is used, measuring the fields as they change. All of the data utilized in this research comes from a network of magnetometers on the Earth's surface, spread about the globe. These instruments allow measurements of both the magnitude and direction of the field at the surface. This chapter will discuss how the magnetometers collected data, introduce the data set, and how it was prepared for analysis.

2.1 Ground-Based Magnetometers

Simply put a magnetometer is an instrument used to measure the strength and direction of a magnetic field [Rasson, 2007]. Many satellites have been equipped with in situ magnetometers for study and observation of the changing field out in space. But prior to the space age, in the early years of magnetospheric research, the main instrument for study was the ground-based magnetometer [Kivelson and Russell, 1995]. Even today a large network of ground station magnetometers are collecting data across the globe, creating a well distributed database in both terms of temporal and spatial resolution. Stations used in this research had two on-site magnetometers: a tri-axial fluxgate magnetometer and a proton precession magnetometer.

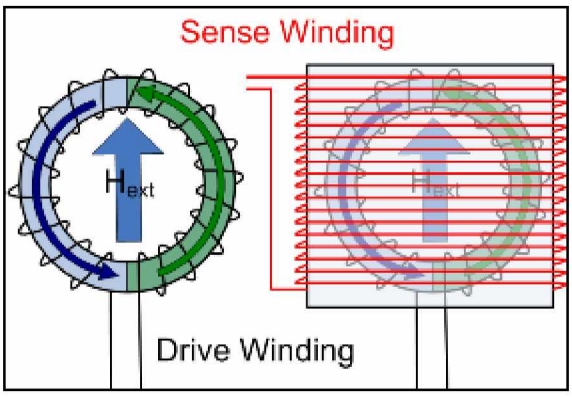

Figure 2.1: Fluxgate Magnetometer [London, 2015]

A tri-axial fluxgate magnetometer is used to determine the individual vector components of the incident field. Described in the Encyclopedia of Geomagnetism and Paleomagnetism, "the flux gate principle uses the nonlinear field/induction relationship of an easily saturable ferromagnetic

core. The core, usually a rod or a ring, is subjected to both the slowly changing external field and an auxiliary AC field produced by a coil and an electronic oscillator"[Rasson, 2007]. The coil is set up to measure the field in the direction of the incident external field H_{ext}, shown as the blue arrow in Figure 2.1. This configuration is for a ring coil, however it can be done with two separate rods as well instead of a single ring. Current flowing through the drive winding can be thought to create two magnetic fields, one in the blue half and one in the green. The resultant fields, one in the direction of H_{ext} and one opposite H_{ext}, in the absence of an external field will cancel out, averaged over time. Since the cores are saturating in sync, there is no change in the net flux of the second coil, shown in red in Figure 2.1, called the sense winding. However, in the presence of an external field, the half core responsible for the field opposite H_{ext} comes out of saturation sooner while the other lags. This creates a net flux in the sense winding, which induces a voltage via Faraday's law. This is reversed later on, creating two voltage spikes. The size and phase of the induced spikes describe the magnitude and direction of field [Evans, 2006].

A proton magnetometer (also known as a proton precession magnetometer) is used to measure the total intensity of the field using Nuclear Magnetic Resonance [Rasson, 2007]. Protons in the presence of an external field will precess around the external field line. The free precession frequency f of protons is described in the Rasson 2007 by the equation:

$$2\pi f = \gamma_p B \tag{2.1}$$

The proportionality constant γ_p, called the gyromagnetic ratio of the proton, is known to a very high degree of accuracy. When enough protons are precessing, a very precise measurement of the strength of the field can be ascertained. These proton magnetometers can be quite compact and have high resolution and sampling rate with typical values of 0.01nT and 3 Hz. This makes them a first choice for automatic and continuous observation around the world [Rasson, 2007].

In order to use, analyze, and interpret the data that is collected from each magnetometer, the coordinate systems the instruments report in must be explained first. There are two main coordinate systems that the reporting stations report in. The first is Cartesian Coordinates (X,Y,Z) shown in red in Figure 2.2. X lies along geographic north, Y along geographic east, and Z normal to the surface directed down. The other system is geomagnetic coordinates, which is a cylindrical

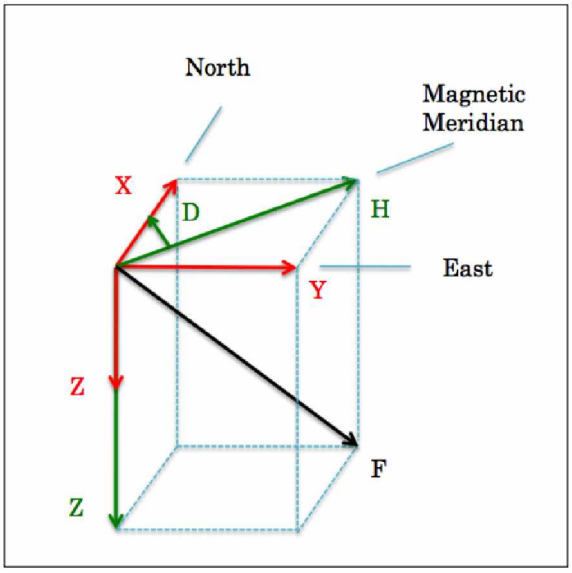

Figure 2.2: Geomagnetic Coordinates [USGS, 2012]

coordinate system with the Earth's surface representing the HD plane displayed in green in Figure 2.2. For geomagnetic coordinates H represents the horizontal component projected onto the plane of the Earth's surface, aligned with the magnetic meridian. The D component is in the direction of declination angle which goes from the magnetic meridian toward the geographic meridian. Z again is normal to the surface, directed downward. It should be noted that in both systems Z is the same. Finally the full field component F, shown in black, represents the full magnetic field vector. The lack of a single standard coordinate system used over the entire time period across all stations led to the need to calculate the missing components. The complete data set was therefore comprised of 6 components: X, Y, H, D, Z, and F.

2.2 INTERMAGNET Data

All of the data for this research comes from the International Real-Time Magnetometer Observatory Network hereafter referred to as INTERMAGNET. This group links with "multiple national organizations across the globe to establish a global network of cooperating digital magnetic observatories, adopting modern standard specifications for measuring and recording equipment, in order to facilitate data exchanges and the production of geomagnetic products in close to real time" [Kerridge, 2001]. As of today, INTERMAGNET has data for 144 magnetic observatories around the world, in comparison to 41 in 1991, the start of the data record. For this particular project,

only North American stations were chosen, with data sets starting without 'major' gaps in 1991 running through 2008. All of the data from INTERMAGNET utilized was taken in the hourly format. This provides a 157,800 hour data log for each station. Nine North American stations were chosen, listed in Table 2.1 and shown in Figure 2.3. The geomagnetic latitudes and longitudes were calculated using the World Data Center for Geomagnetism, Kyoto converter for the year 2000, as this represented the median year in the set. This was necessary since geomagnetic coordinates are in reference to the magnetic pole, which changes position every year in contrast to the stationary geographic pole. Geomagnetic coordinates were chosen as it was thought the signals in the data would be related to magnetic field lines of the magnetosphere and therefore a coordinate system of latitude and longitude based on the magnetic field seemed the best choice. The author would like to thank the national institutes that support the observatories and INTERMAGNET for promoting high standards of magnetic observatory practice and their involvement in this research.

Table 2.1: Magnetometer Observatories

Name	Abbreviation	GeoMag Lat (N)	GeoMag Long (W)
Thule	THL	87.8	13.7
College	CMO	73.8	114.1
Ottawa	OTT	55.7	3.7
Newport	NEW	57.8	55.7
Boulder	BOU	48.3	39.7
Fresno	FRN	43.4	55.1
Tucson	TUC	30.0	42.5
Honolulu	HON	21.5	90.5
San Juan	SJG	28.4	-5.8

Table 2.1 is arranged by geomagnetic latitude as this convention was used throughout the analysis for the base ordering of stations for the cross correlations. The convention was necessary as when running a cross correlation the signal of one station is correlated to another by comparing each data point from one signal to those of the other signal, shifted by some time step. For analyzing the cross correlation plots the data to the left of the y-axis, the negative time values, represent the northern signal leading the southern. Likewise, right of the y-axis or the positive time values, the southern signal is leading the northern. This will be elaborated in Chapter 3's description of the cross correlation of method.

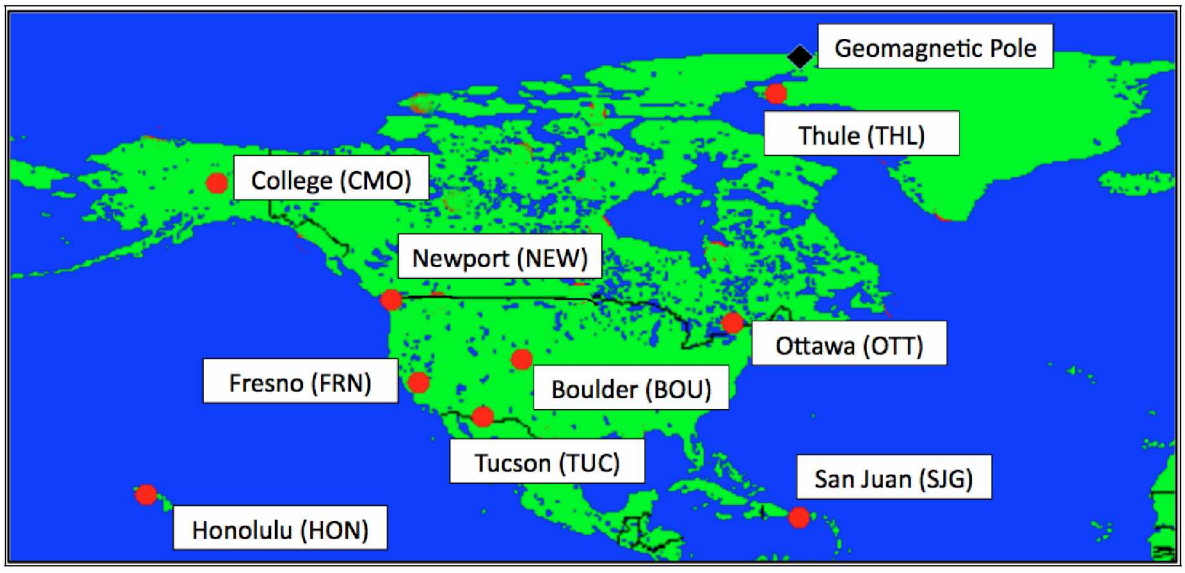

Figure 2.3: Magnetometer Observatories
Adapted from INTERMAGNET IMCDVIEW Software

While most of the stations are on United States territory, there are two stations on other countries, Ottawa in Canada and Thule on the island of Greenland, part of the Kingdom of Denmark. Originally Resolute Bay (Canada) and NASA Stennis (USA) were also chosen, but were removed due to data issues. Resolute Bay's record began in 1992, a year after the rest and NASA Stennis had a larger amount of error data in comparison to the rest of the stations. The data was stored on CD's sent by INTERMAGNET , split into individual years or half years. North American stations were chosen since they represented a decent range in both latitudinal and longitudinal coordinates. The original 1991 data set only covered the European region with a similar spatial coverage. As there were only 41 stations to begin with in 1991, the North American stations utilized represent about a quarter of the available data. The largest range in geomagnetic latitude, about 60 degrees, was between Thule and San Juan. The largest difference in geomagnetic longitude was about 120 degrees, between San Juan and College. This subset of all the North American stations give a fair representation of data across the majority of the continent. From each of these stations, the data record for every component was taken and run through several data preparation steps before starting analysis.

2.3 Data Preparation

Figure 2.4 and Figure 2.5 depict two examples of the raw data signals. The data range for both plots are equal, 4000 nT, in order to compare at the same scale. Easily evident in the Boulder plot is a linear trend while College's plot displays a strong periodicity. In fact, all of the components for all stations had a linear trend and multiple periodicities, but as shown the dominance of the features varied between stations and components. The possible sources for both the trend and the periodicities will be discussed later on in this chapter. The data preparation method was developed to remove the trends, means, and periodicities present in the data as per the requirements of the analysis methods. It should be noted that the error flag for missing data has been removed from the plots above, as explained later in this chapter.

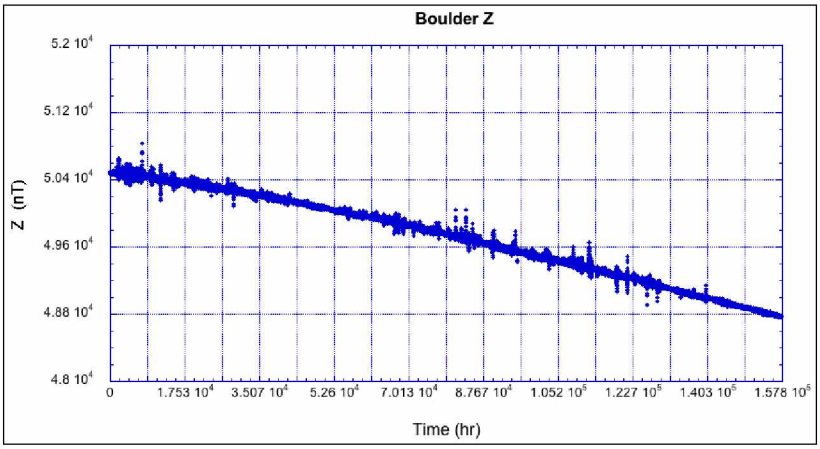

Figure 2.4: Raw Data: Boulder Z Component

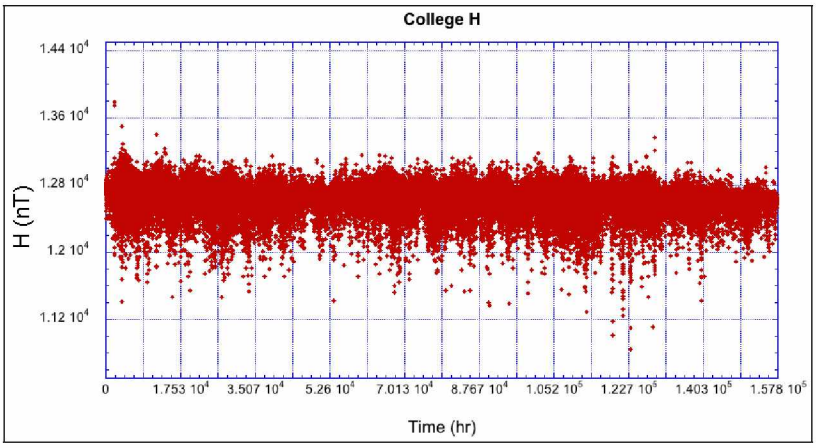

Figure 2.5: Raw Data: College H Component

There were several stages of adjustments needed in preparation for analysis with the data. The American stations reported in geomagnetic coordinates (HDZ) up until 2004 when they switched to Cartesian whereas Ottawa and Thule were Cartesian all along, requiring calculation of the missing components for each station. Error values from times when the instrument's recording was interrupted due to maintenance or interference, needed to be replaced so that the overall signal was intact. A linear trend thought to be linked to the changing position of the magnetic pole needed to removed. The largest hurdle in data preparation was the presence of multiple periodic signals in the data. These had to be removed without sacrificing the consistent time step or the phase of the data, especially for the Rescaled Range (R/S) Statistic analysis. By the end of the data preparation process, the aim was to have the data cleaned, demeaned, detrended, and deperiodized of all the periodicities.

For this work, programs were written in three different languages to suit different needs. For most of the data preparation, programs were written in the National Center for Atmospheric Research (NCAR)'s relatively new NCAR Command Language (NCL). This script based language was mostly designed for work with NOAA and NASA databases, but was chosen as an extension of the main researcher's background in Atmospheric Science. NCL has many built in algorithm and features, such as random number normal distribution generators or linear regressions. The analysis programs for the Probability Density Function (PDF), R/S Statstic, and Cross Correlation were written in FORTRAN 95 or updated from FORTRAN 77. FORTRAN is a robust language that works well with large quantitative calculations and has a very mature compiler. This gave great power for debugging any issues within the complex analysis codes. For quick scripting needs such as data formatting or organization, Bash scripts were used.

The first challenge was dealing with error code data, where an issue with the data point was represented by 99999. There were various causes that could have triggered this message. Some of these included the instrument turned off for maintenance or replacement, overload in the circuits, and interference. The 9 stations had 18 years of continuous hourly measurements which equates to 1,420,200 data points, roughly 5 percent of which was an error value. This was deemed an acceptable amount of error, provided missing values were dealt with in such a way that the data record's form was not largely impacted. The missing values had to be removed by some means or no analysis could be done, as all three methods would have displayed false signals.

Several methods for this data cleaning were considered and compared. The first was to pull the data points that were missing values and concatenate the 'snips' together. This, however, would create a data record with an inconsistent time step, which was not optimal for analysis. The second was to replace the missing values with zero, essentially demeaning the missing values. This would still have created a false trend in the analysis. Next considered was replacing the error flag value with the immediate preceding value. This would result in flat lines of data, but would keep the rough overall progression of the signal intact. While not optimal, it would keep a constant time step and could be demeaned later on in the process. An improvement upon this approach was to average the value immediately prior and following a missing value or block of missing values. This still introduced an extra trend, but was considered more reasonable as it better matched the signal. Issues did arise for data records that started or ended with missing values, rectified by filling in with the value preceding or following, as the situation demanded.

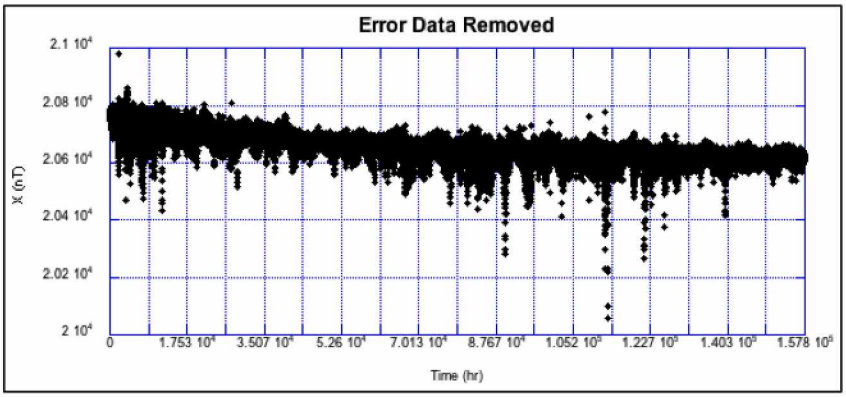

Figure 2.6: Data Cleaning: Error Data Removed

As shown in Figure 2.6 there was at least one major linear trend evident in the data, which was linked to the movement of the geomagnetic pole. A linear regression algorithm built into NCL was utilized to remove the major trend as well as demean the data. The command regline, "computes the information needed to construct a regression line: regression coefficient (trend, slope,...) and the average of the x and y values" [NCAR, 2015]. Demeaning and detrending is an integral step necessary for all three analysis methods. By subtracting out the line created from regline, the data was demeaned and detrended together. Figure 2.7 shows the results of the demeaning and detrending process. The data is now centered at zero and has had the linear trend removed.

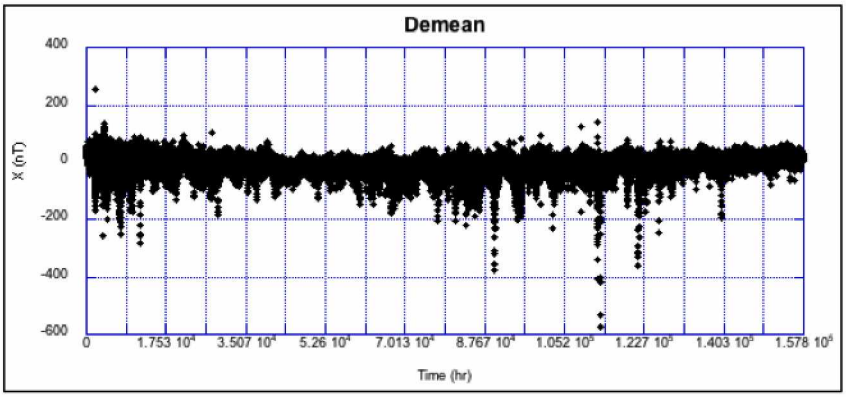

Figure 2.7: Data Cleaning: Demean and Detrended

There were four main periodicities identified in the data set: a 10-14 year cycle, an annual, a weekly to monthly, and a diurnal. Before these could be removed, the drivers of these periodicities were investigated. The large 10-14 year cycle seems to match well with the sun spot cycle, discussed later in the chapter. The annual periodicity is thought to be an emergent property of the Earth's orbit and how the slight eccentricity changes the relative location in the Sun's magnetic field. The week to monthly scale periodicity was originally thought to be a single signal, possibly related to the lunar orbit or the Sun's rotation. However, based on characteristic signals evident in the analysis, it seems there are a collection of multiple drivers and signals, not a single periodicity. As mentioned in Love and Rigler [2014], several magnetic oscillations have been linked to currents created due to changes in the atmosphere and ocean, as well as the lunar tides. However, this conclusion came after data analysis as an explanation for the signals seen in the plots. Only a single monthly deperiodizer was created which was unfortunately ill suited to removing the collection of weekly to monthly periodic signals. The diurnal cycle was easily identified as the orientation of the magnetometer station was dependent on its location on the Earth's surface as it rotated.

The typical method for removal of periodic variations in magnetic data is by using a Fourier Transform and filtering in frequency space. However, this could not be utilized due to the sensitivity of the analysis methods to the phase of the data. By removing a frequency in frequency space and then inverting the transform, the signal can be shifted, leaving the phase of the data changed. This is due to the fact that the transform assumes an infinite time series and perfectly periodic signal, which is not true for our data series. Our analysis methods require the phase remain unchanged. Therefore a different method was devised which would maintain the phase, a periodic averager.

The theory of a periodic averager is fairly straightforward. Assuming a perfectly periodic signal, averaging the data values for the same time in each cycle should remove the periodic envelope leaving only the perturbations. For example, in the diurnal deperiodizer, every data point that corresponded to noon was averaged. Then that average was divided out of each data point that corresponded to noon. This would remove the mean value at noon which should be the result of the periodic signal, only leaving the variations that come from individual events. In order to ensure the averages would never be zero, which would lead to division by zero, the absolute value of the data was taken first. Analysis of the perturbations that remained after removing the periodic signals was the aim of the research, in order to better understand the frequency of the different nonperiodic events.

For the diurnal periodicity this methodology worked well, but the presence of leap days cause major issues for both the monthly and annual deperiodizer. Since the periodic averager sought to average each January 1st, October 31st, or November 5th together, the presence of a non-constant February 29th created issues. Originally, an attempt to simply average the 5 leap days together (1992, 1996, 2000, 2004, and 2008) was made. However, this led to large spikes in the February month. After consideration, the decision to simply remove the 120 data points was made. This did, as with the removal method of the missing values affect the continuity of the data set, as the time step now had gaps. The impact of 120 data points versus 1.4 million, however, was determined negligible enough to ignore.

Dimensional analysis of the methodology was performed and showed that after the first deperiodizer, the data had been normalized. This is due to the division of the average. While this has little impact on the cross correlation or R/S analysis, it does mean the x axis of the PDF, the bin values, are unitless. As such, the PDF can be considered normalized to the scale size of the perturbation.

For validation of the data preparation methods, an artificial data set was created as a test. The data signal contains two periodicities: one of a daily 24 hour period and one with a 8760 hour period, which represents the annual periodicity. A simple linear trend was added to mimic the pole movement. An array of randoms number, called nd, generated by a normal distribution added noise for the signal as shown in Equation 2.2 and Figure 2.8 below. The signal was demeaned, detrended, and deperiodized via the data preparation program.

$$y(x) = nd(x) + 1000 \sin\left(\frac{\pi}{24}x\right) \sin\left(\frac{\pi}{8760}x\right) - \frac{x}{50} \tag{2.2}$$

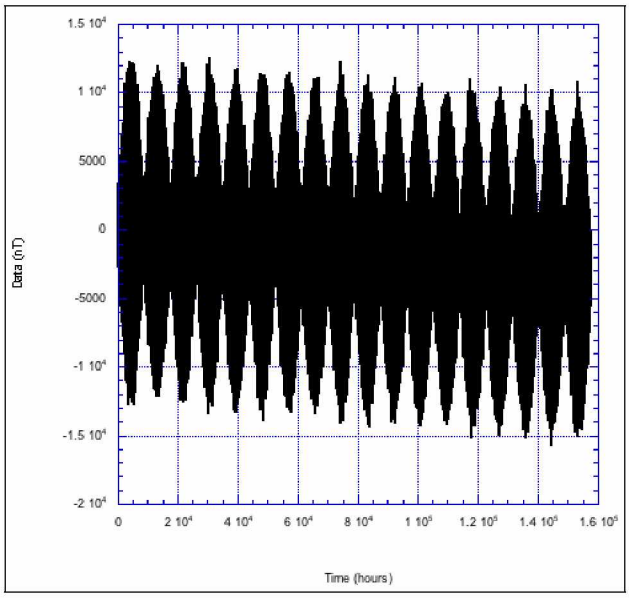

Figure 2.8: Artificial Test Signal

A flaw in the deperiodization methodology was discovered from the validation test. As the deperiodization process is a periodic averager, an average of all data points corresponding to a specific time is calculated. Then all data points corresponding to said time are scaled by that average, attempting to remove the envelope of the periodic function. However, if the periodic signal is not uniform, there may be a large spike introduced into the result. If the periodic signal is not perfectly periodic it appears that one cannot match the same point on each cycle as a cycle's length is varying. At the maximum amplitude of the periodic signal there appeared little to no impact, since the ratio of the data to the average is small. At the minimum in the periodic signal, however, there will be a large impact since shifting the averages slightly will lead to a larger number being divided by a small average. This accounts for why the spikes seen in the plots happen at the end of the years as seen below in Figure 2.9b. What was also noted, was the magnitude of the periodicity had been reduced by several orders of magnitude, also seen in the Figure 2.9b. This suggests the deperiodizer was successful in removing the magnitude of the signal but possibly artificially introduced a periodicity with these endpoint spikes. As this flaw was due to the methodology, each deperiodizer was unsuccessful in fully removing the periodic signal it was designed to.

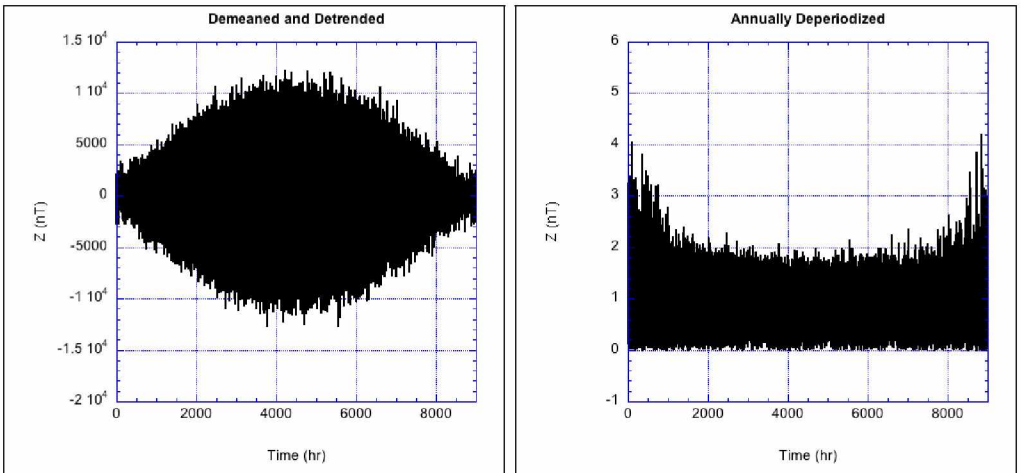

(a) Before Annual Deperiodizer (b) After Annual Deperiodizer

Figure 2.9: Comparison of Signal Before and After Annual Deperiodization

While the full periodicity was not removed, the analysis methods were still applied to the data. The next chapter will introduce the Probability Density Function, R/S Analysis, and Cross Correlation analysis methods, including their theory, implementation and the goal in using each. Understanding how the periodicities would affect each different method and the interpretation of the results was important before analysis, so that interpretation of nonperiodic signals could be done. How each method was impacted is discussed later in Chapter 4.

Chapter 3 Analysis Methods

The focus of this research was to look at spatial and time signals in the magnetometer network for interesting and useful relationships. In particular of note, nonlinear relationships would represent a useful start for risk analysis of space weather. To that end three main types of analysis were conducted in the aim of probing the interactions between the stations. Cross correlation was performed to look for latitudinal and longitudinal dependence, lead and lags in signals, and vector dependence in the magnetic field. The probability density function (PDF) analysis was utilized to look for temporal memory in the system, identify regions of different driving mechanisms, and look at the probability of different scale size events. Of particular interest is the probability of the largest scale sizes. R/S analysis was performed as an indication for the presence of self-organized criticality (SOC) and also for long term time correlation in the system.

3.1 Cross Correlation

The cross correlation process involves measuring the similarity of two different signals. One of the most useful aspect of the correlation comes from identifying a lead or lag in the signal. This can infer a causal link, though of course not all correlations are causal. It can also indicate a predictive pattern via a temporal or spacial preference. For example, there would be a lead in the temperature signals going from west to east as a cold front passed. This would indicate the front's passage in direction and could also be used possibly to predict changes in the station ahead of the front. Due to the lead/lag nature of cross correlation, the order of which the correlation is done matters. The data corresponding to the negative time values in the plots displaying when the northern signal led the southern. Right of the y-axis, the southern signal was shifted ahead of the northern. This allows for examination of the lead/lag nature with ease.

An autocorrelation is when a cross correlation is taken of a signal with itself. It must, by definition, have a starting amplitude of 1. The autocorrelations in this paper were used as a test of the methodology and to set a baseline to compare the cross correlations to. Figure 3.1 depicts Boulder's autocorrelation for the X component of the magnetic field. From this, we see a peak starting at correlation value 1 which quickly falls off toward zero, being dominated by the diurnal periodicity after 20-30 hours.

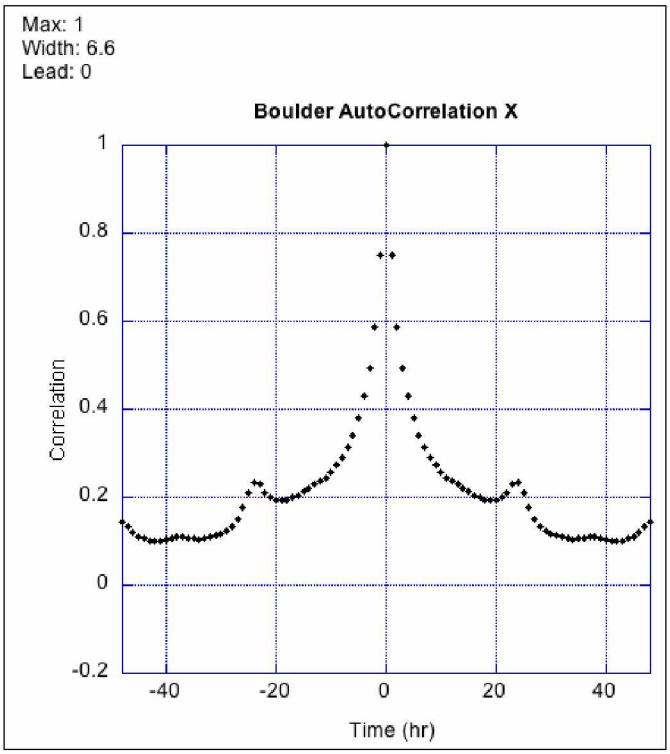

Figure 3.1: Boulder Autocorrelation X Component

The general form pf the cross correlation equation used in this research is shown in Equation 3.1 where $\overline{x}$ and $\overline{y}$ represent the respective means for those data sets and d is the delay value. Essentially, the delay value shifts the data so only part of both arrays are being correlated at any one time.

$$\frac{\sum \left[\left(x\left(i \right) - \overline{x} \right) \left(y\left(i - d \right) - \overline{y} \right) \right]}{\sqrt{\sum \left(x\left(i \right) - \overline{x} \right)} \sqrt{\sum \left(y\left(i - d \right) - \overline{y} \right)}} \tag{3.1}$$

For each cross correlation, the plot was analyzed for 4 different values. The maximum amplitude describes the maximum correlation value for the signal. This is a good indication of the starting strength of the correlation, allowing for analysis of how strongly the initial correlation of two stations was dependent on their proximity to each other. The half amplitude time values represent at what time value (x-axis) the correlation first reaches a value equal to half of the maximum amplitude (y-axis). This can give an indication of temporal memory in the system; how long the signals stay correlated. The full width at the half maximum amplitude allowed for comparison between different cross correlations, taken by measuring the distance between the left

and right half amplitude time values. Finally, if there was a lead or lag in the peak, this was recorded.

An example of a cross correlation plot is shown in Figure 3.2. The two stations being considered are Ottawa and San Juan. As Ottawa is the more northern station, Ottawa leads San Juan left of the y-axis while San Juan leads Ottawa right of the y-axis. The numbers in the top left corner represent the maximum amplitude, the two widths at half maximum amplitude time values, the full width at the half maximum amplitude, and the lead/lag value. Due to the leftover periodic signature that remained after the data cleaning, we see a strong periodic correlation in most signals. Also for ease of analysis, plots have been focused in on the center-most peak, though looking how the correlation changes over the full time record is also of interest. For this example, we see a fairly weak starting correlation of .2244 lagged by 4 hours. The full width at the half maximum amplitude of 18.6 is a moderate value in comparison to the data set. We see at t = -24 and t=24 a bump representing the presence a diurnal periodicity. Figure 3.2 depicts the maximum amplitude as the green line, the full width at half maximum as the purple line, and the lag as the red line for reference.

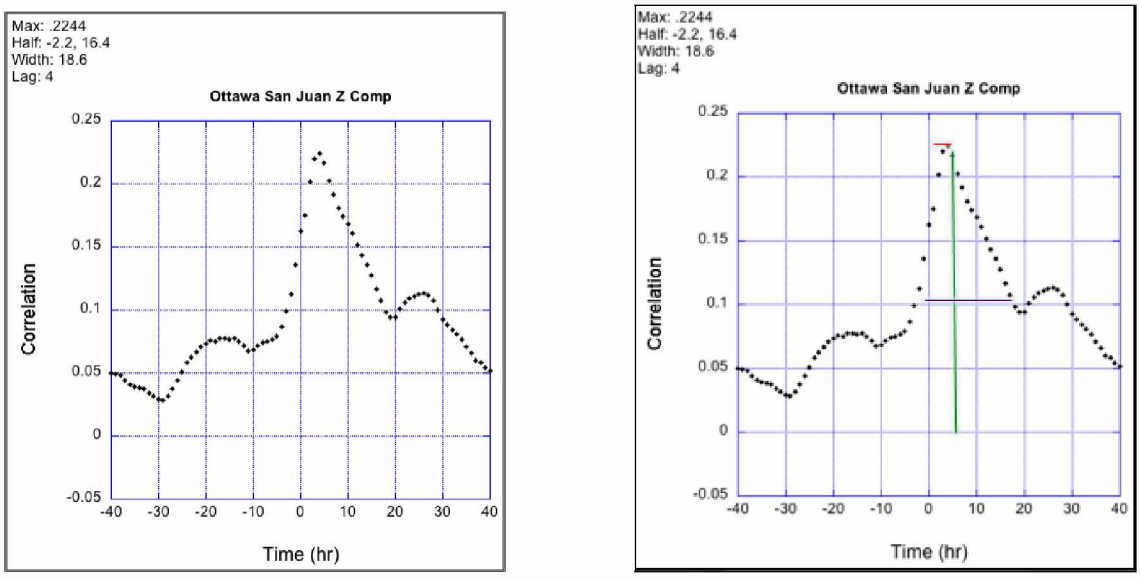

Figure 3.2: Example of a Cross Correlation Plot: Ottawa San Juan Z Component

The values from all the cross correlation plots were tabulated and plotted versus three distances: the geomagnetic latitudinal difference to show any potential north-south dependence; the geomagnetic longitudinal difference to show any potential east-west dependence; and the central

angle, a measure of the angular distance between stations. The central angle was calculated using the stations' geomagnetic coordinates and the spherical law of cosines as shown in Equation 3.2.

$$\Delta\sigma = \arccos\left(\sin\phi_1 \sin\phi_2 + \cos\phi_1 \cos\phi_2 \cos\Delta\lambda\right) \tag{3.2}$$

where ϕ represents geomagnetic latitude, $\Delta\lambda$ represents the difference in geomagnetic longitude, and $\Delta\sigma$ is the central angle or angular distance between the two. A positive latitudinal difference, $\Delta\phi$, represents a northern station subtracting a southern one, such as College (73.8 N) minus Tucson (30.0 N). For a positive longitudinal difference, $\Delta\lambda$ a more western station would be subtracting a more eastern one, such as Honolulu (90.5 W) minus Boulder (39.7 W).

3.2 Probability Density Function

The Probability Density Function is a common tool in time series analysis that describes the probability of a data point being at a certain value. The integral of the function summarily must be equal to 1. In this approach, the function is split into a certain number of divisions, called bins. A variable bin width is utilized to avoid bins with too few data points in them. This is done by requiring a minimum amount of data points to be in a bin before the next bin is created, reducing some of the noise for the largest scale size events.

First the PDF is generated for uniform bins. Then each bin is evaluated to see if the number of events in each bin is less than some threshold value, in this case 100. If not, the events are added to the next bin. The process starts in the center and works out so that larger bins are added to smaller bins. The PDF calculation is described by Equation 3.3

$$\frac{1}{N} \sum_{n=1}^{x_{total}} n\left(x_i\right) \Delta x_i \tag{3.3}$$

where n represents the total events in bin x_i, N is the total number of events, and x_{total} represents the total number of bins.

Many PDF plots follow a Gaussian curve, having a large number of data points in the center of the range, falling off toward the ends. As the PDFs here are plotted on a log log scale, a Gaussian curve would be represented by an exponential slope. Examining for a power law slope, a straight line on a log log plot, was the main focus for interpretation. A slope greater than -2

is of particular interest. It would indicate a Levy distribution and could indicate an area of self-similarity. Self-similarity in a system means at multiple scale sizes the characteristics of the signal are the same, much like examining the shape of a fractal. For this analysis, the power law equation displayed will only represent a region of the curve rather than the whole curve.

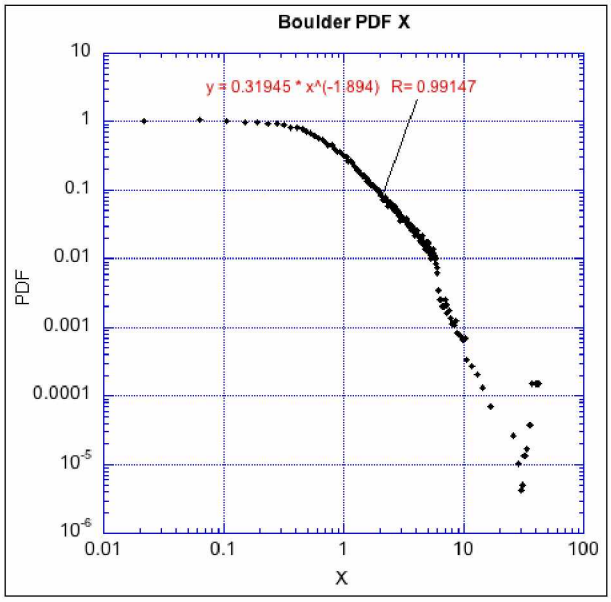

Figure 3.3: Example of a Probability Density Function Plot: Boulder X Component

Figure 3.3 shows an example of a PDF plot with a power law. As shown by the equation, there is a region starting near x = 1 with a power law of -1.8, representing an area with a Levy distribution as compared to a Gaussian. There also is a suggestion of a power law in the tail or end of the plot. A power law here is indicative of a 'heavy tail' which represents increased probabilities of large scale events. This is evident if the probabilities for these largest scale events are greater than those of a Gaussian curve. In risk analysis this can be an important element in identifying the system's temporal memory as well as estimating the impact of larger events. For example, if in a forest fire model there was evidence of a heavy tail this could indicate the larger, more destructive fires may occur more frequently than expected. This could infer that the preventive measures implemented for the smaller fires were actually increasing the likelihood of larger ones. A real world demonstration of this effect was shown in the method of using small fires to remove brush and other fuel to reduce the amount of fires. In doing so, however, it created a system in which when fires did occur, there was a higher probability of them being high impact. In the same

way, a heavy tail could indicate in the magnetometer system that a particularly strong magnetic event could leave a higher impact and a longer effect in the system than predicted.

3.3 R/S Analysis

The Rescaled Range Analysis, also known as R/S, is a time series analysis tool that measures long term memory in a series. Described in Price and Newman [2001] "the rescaled range (R/S) analysis pioneered by Mandelbrot and Wallis (1969)... can be used to demonstrate the scaling behavior associated with self-organized systems". Self-organized criticality (SOC) cannot be proven via the R/S Analysis, but it can be used as a strong statistical indication of the presence of SOC behavior. R/S analysis is one way of calculating the Hurst exponent, though not the only one. The R/S can be used to see how events in the past a different times affect the events of today. That is, if the system has memory of past events that influence the present. The Hurst exponent is calculated via Equation 3.4:

$$\frac{R}{S} = s^H \tag{3.4}$$

where R is the sample sequential range, S is the square root of the sample sequential variance, s is the sample size, and H is the Hurst exponent.

The exponent will vary from 0 to 1, with three main categorizations. A Hurst exponent ranging from 0 to 0.5 represents a very coherent process with anti-correlation, which will be stronger the closer to 0 the exponent is. Likewise an exponent ranging between 0.5 and 1 represents a very coherent process with correlation, again stronger near 1. An exponent of 0.5 represents a wholly stochastic process lacking correlation or coherence [Price and Newman, 2001]. From this, we can observe, over a set range of data, areas of strong correlation, anticorrelation, or no correlation. Of particular interest for this research is the Hurst exponent at very large time scales (years to decades) looking for long term correlation in the system. The exponent will be equivalent to the slope of the log log plot shown in Figure 3.4.

R/S analysis is very sensitive to periodicities. At a time value equal to the period of a periodicity, the slope will change drastically from strongly correlated to strongly anticorrelated. The region near this cusp is dominated by the periodicity, burying any signals related to perturbations.

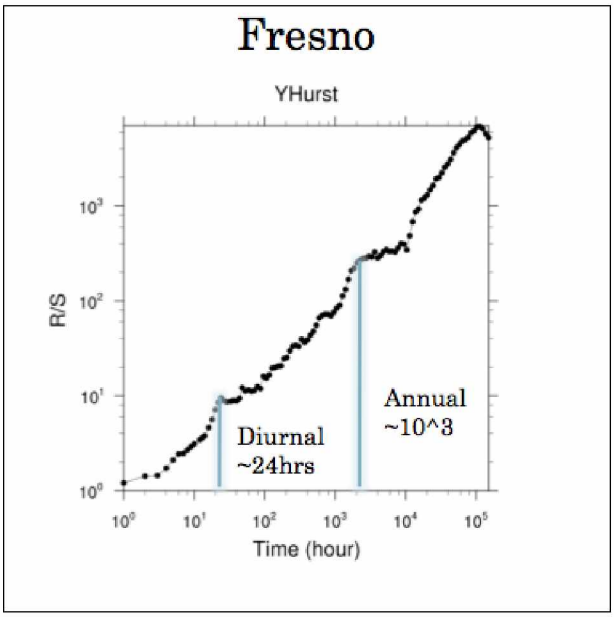

Figure 3.4: Example of a R/S Analysis Plot: Fresno Y Component

As seen in Figure 3.4 there are many periodicities present in the data. Also present are areas where the exponent goes negative. These are not thought to be accurate to the data, but are artifacts of the method. Even with the problematic regions of the graph, there still may be some areas of interest that could be indicative of SOC and long term memory.

Chapter 4 Results

This chapter will present the results seen after analysis methods were applied. The cross correlation analysis looks at spatial correlations, looking for latitudinal and longitudinal dependencies. It also deals with some estimation of correlation length of events. The Probability Density Function analysis examines the frequency of events at different scale sizes, aiming to understand if certain scale sizes demonstrate self-similar behavior. PDF analysis also attempts to identify regions that are driven by different mechanisms in the Sun-Earth system. The Hurst R/S analysis investigates the temporal correlations and memory of the system.

4.1 Cross Correlation

The cross correlations were performed for all 9 stations and each component. Only same components were correlated (i.e. X with X, Y with Y) and autocorrelations were performed to verify the process and set a baseline for comparison. From each plot the maximum amplitude, full width at half maximum amplitude, and lead/lag were recorded and then plotted vs geomagnetic latitude difference, geomagnetic longitude difference, and central angle as defined in Section 3.1 and Figure 3.2 of the previous chapter. Analysis of these plots revealed several latitudinal and longitudinal dependencies, discussed in this chapter.

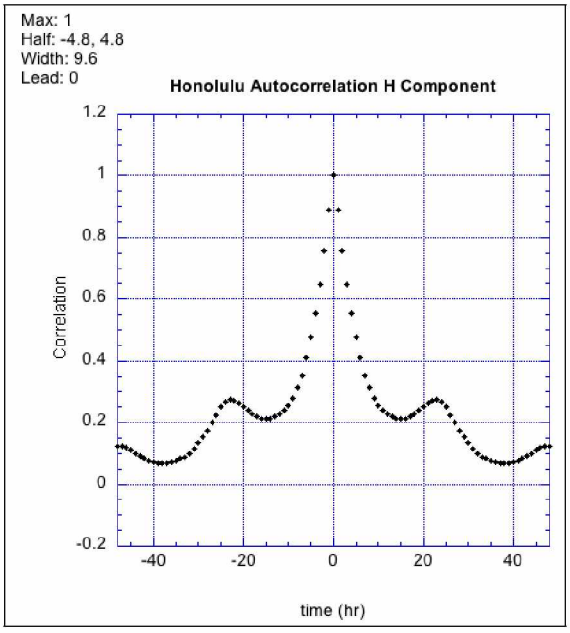

Figure 4.1: Honolulu Autocorrelation: H Component

The autocorrelations for all components showed similar plots as shown in Figure 4.1. As expected, the maximum amplitude is equal to one across all stations and components. The main peak falls off quickly, eventually oscillating near the axis with a daily periodicity. The autocorrelations showed the thinnest full widths at half maximum amplitude as compared to the cross correlation plots. There was no lead or lag value, as would be expected when correlation a station with itself. The autocorrelations create a baseline for the cross correlation plots to be compared to.

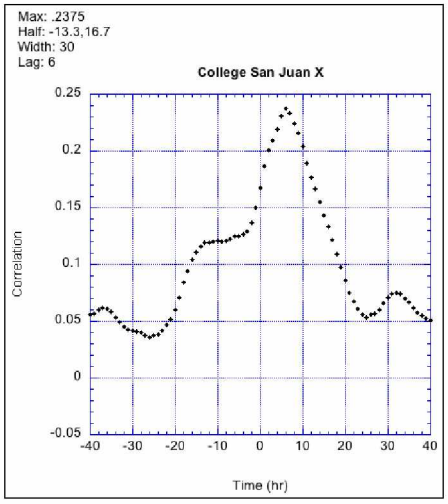

Figure 4.2: College San Juan Cross Correlation: X Component

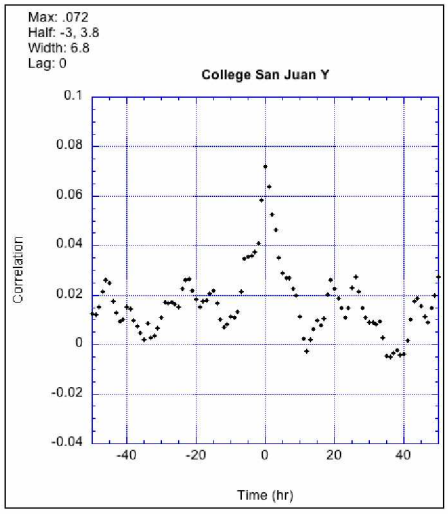

Figure 4.3: College San Juan Cross Correlation: Y Component

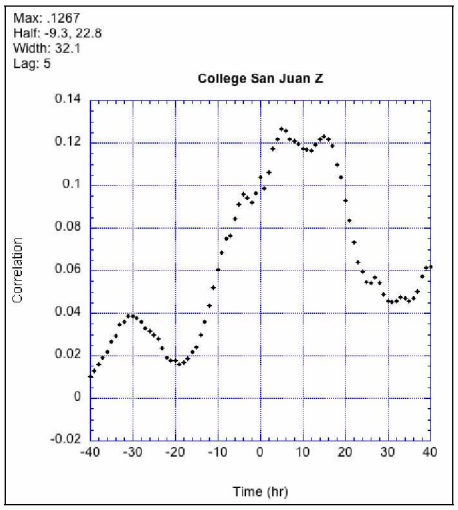

Figure 4.4: College San Juan Cross Correlation: Z Component

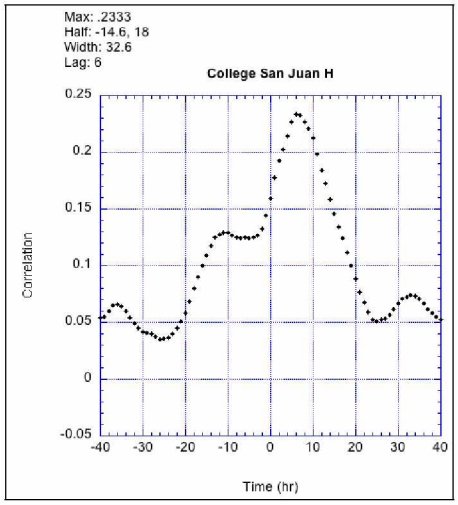

Figure 4.5: College San Juan Cross Correlation: H Component

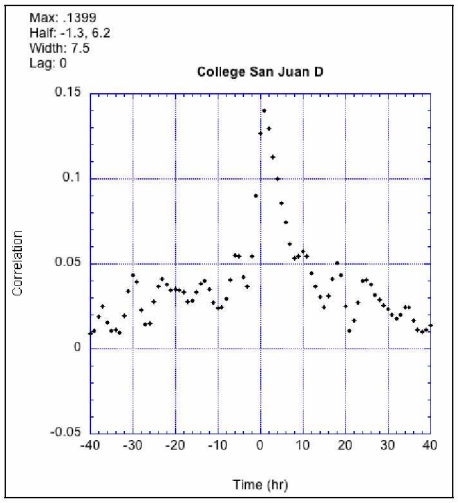

Figure 4.6: College San Juan Cross Correlation: D Component

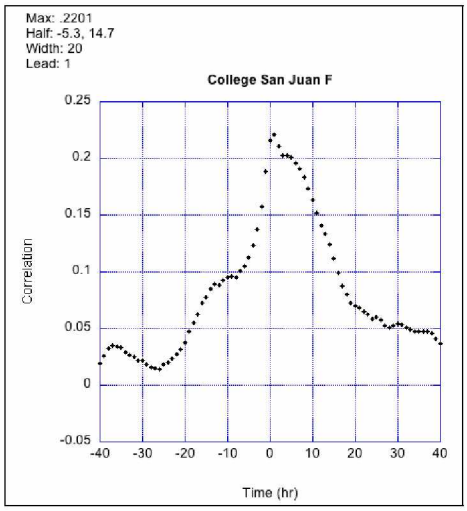

Figure 4.7: College San Juan Cross Correlation: F Component

Figures 4.2 to 4.7 represent the 6 components of the College San Juan cross correlation, chosen as it has one of the largest separation distances of the data set both in terms of geomagnetic latitude difference, 45.4 degrees, and longitudinal difference, 119.9 degrees. As seen in all 6 plots the correlation starts at a peak value and falls off rapidly, oscillating near the axis with a rough daily periodicity. Each component's maximum amplitude were under 0.25, representing a fairly weak starting correlation as compared to many other pairings in the data set. By comparison, some of the maximum amplitude values for other stations were as high as 0.8, as with the Fresno Tucson. This suggests that maximum correlation values are weaker over larger separation distances. Also of interest, the H and X components had stronger maximum values compared to the longitudinally aligned Y and D, suggesting a stronger latitudinal bias. The full widths of the H, X, and F components were fairly large: X - 19hrs, H - 16hrs, and F - 20 hrs. The longitudinal components, by comparison, were almost an order of magnitude smaller: Y - 4.4hrs, D - 2.5hrs, with the vertical component falling in the middle with a value of 12.5 hrs. These represent the length of time the stations' signals stay correlated, a possible indication of the memory in that system. There is a common occurrence in the analysis of the X and H components having similar behaviors as well as the Y and D components. This seems logical as X and H are both roughly in the north-south alignment while Y and D are more in a east-west alignment. X, H, and Z all showed noticeable lag values of 5 or greater compared to the other components, possibly indicating that the signals

from the southern station lag behind those of the northern stations. This could hint at how signals propagate in the network, starting from the north and heading south.

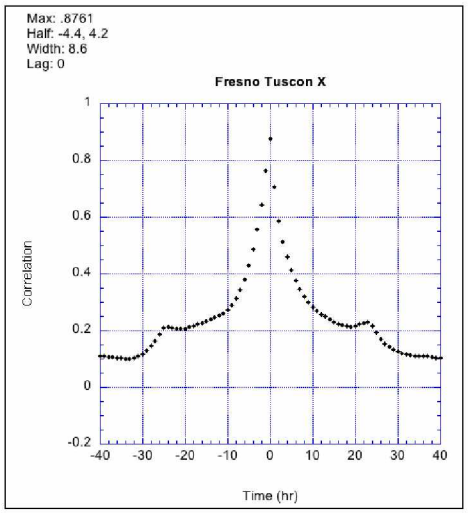

Figure 4.8: Fresno Tucson Cross Correlation: X Component

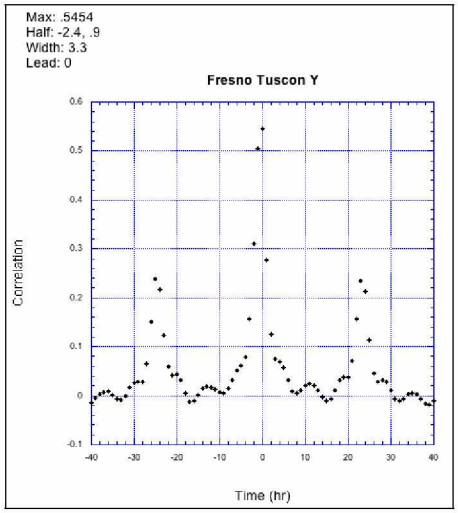

Figure 4.9: Fresno Tucson Cross Correlation: Y Component

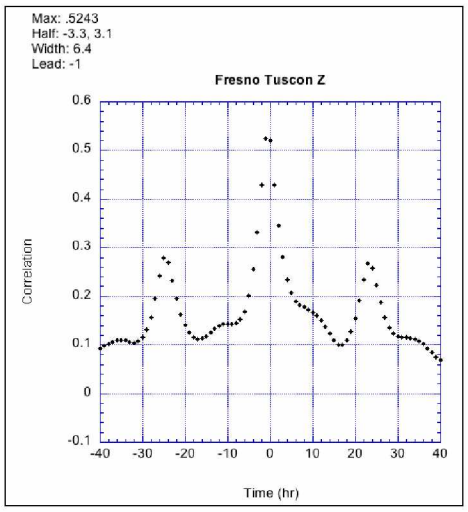

Figure 4.10: Fresno Tucson Cross Correlation: Z Component

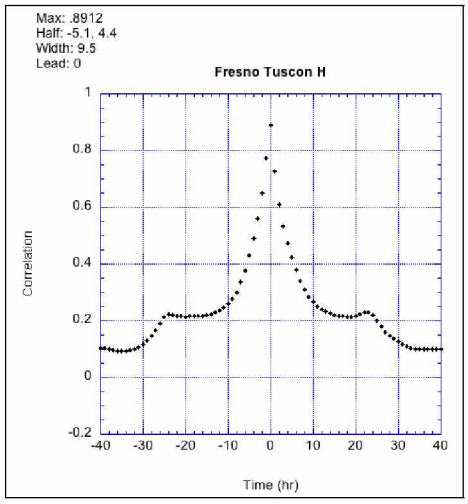

Figure 4.11: Fresno Tucson Cross Correlation: H Component

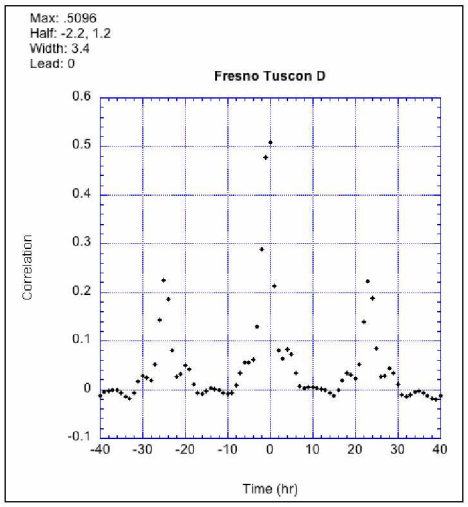

Figure 4.12: Fresno Tucson Cross Correlation: D Component

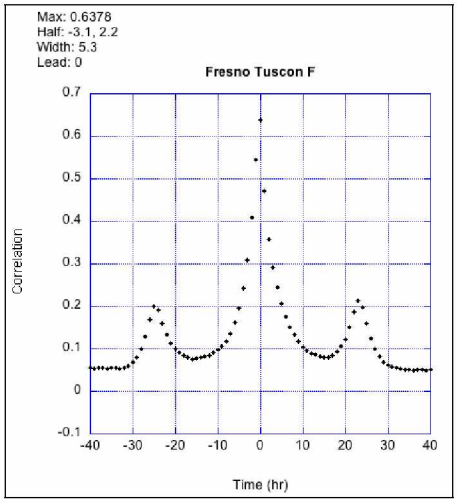

Figure 4.13: Fresno Tucson Cross Correlation: F Component

As a comparison to the College San Juan plots, Figures 4.8 to 4.13 show the Fresno Tucson cross correlations. Fresno and Tucson are the closest in terms of distance in both geomagnetic latitude and longitude of the station pairs. This is the other extreme as compared to the College San Juan. The maximum amplitude values are much higher ranging from around 0.5 to 0.9. This would be expected for stations in close proximity to each other if there was both local and nonlocal natures in the signals. The full widths at half maximum, however, are smaller ranging from 3.2 hrs to 6 hrs. This could indicate the signals lose correlation faster than College San Juan, that the periodicities are more dominant here, or that the magnitude of the maximum correlation is

inversely proportional to the width. The X and H components have stronger amplitudes and wider full widths than the longitudinal counterparts. As with Ottawa San Juan, this suggests a stronger latitudinal connection.

After tabulating all maximum amplitude, full width at half maximum, and lead/lag values for all plots, each variable was plotted versus 3 separation distances: geomagnetic latitude difference, geomagnetic longitude difference, and central angle. These different directional separations allow for examination of field aligned and non-field aligned phenomena. Beyond looking for the existence of local behavior, there could be specific directional components that link to certain waves in the magnetosphere. A short description of each result and possible interpretations of features follow.

The maximum correlation values saw a definite difference between latitudinal, Figure 4.14 and longitudinal dependence, Figure 4.15. In the latitudinal case, the stations closest together have the strongest maximum amplitude. This falls off with an average slope of -0.1 to -0.2, though not all plots were purely linear. The H and Z components show the most linear trends, with X deviating slightly from linear. Y and D show a less organized relation to latitude, which would make sense as they are more tied to longitude. The H component, as seen in Figure 4.14, having the strongest trend is expected as it is directly aligned with the geomagnetic latitude. The Z component, however, is thought to be independent of any horizontal dependence, so as to why that has such a strong response is unknown. It is possible the Z component is somehow tied to the horizontal components.

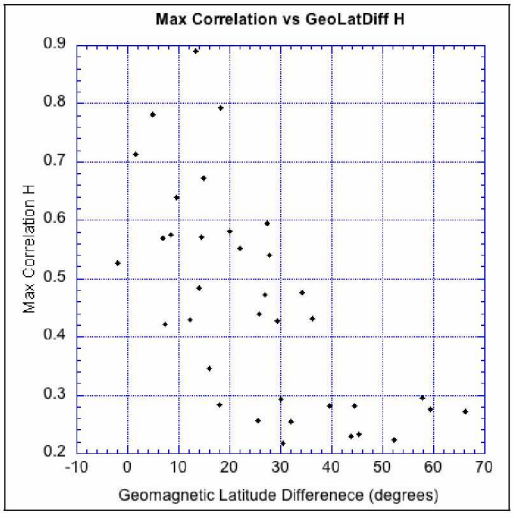

Figure 4.14: Maximum Amplitude vs Geomagnetic Latitude Difference: X Component

For the maximum amplitude vs longitude plots, as shown in Figure 4.15, a similar relationship as with the latitudinal case is seen. For all components, the plots are centered at 0 and triangular in shape, with the peak near 0. The correlation values fall off the farther away stations are in longitude in both directions, just as with latitude. This is especially strong in the Y and D components, as would be expected as they lay in the longitudinal direction. As the ordering of the pairs was based on latitude not longitude, some of the cross correlation plots would have negative longitudinal differences, whereas the convention ensures there cannot be a negative latitudinal difference. This gives rise to the triangular shape shown in Figure 4.15. So while the shape of the plot here is different, the relationship is the same: the closer the stations are the stronger the maximum amplitude.

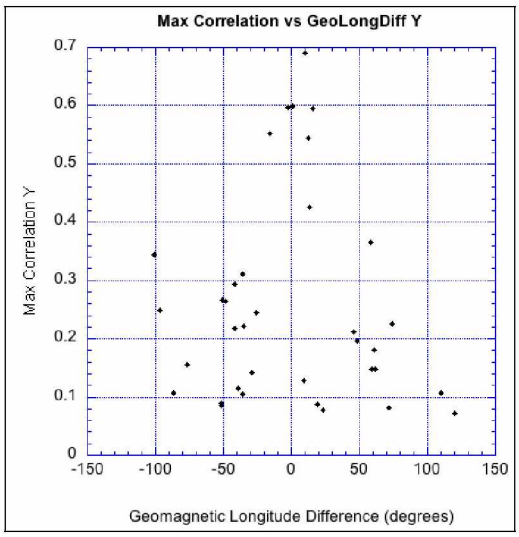

Figure 4.15: Maximum Amplitude vs Geomagnetic Longitude Difference: Y Component

The maximum amplitude vs central angle plots, as shown in Figure 4.16, mimic the shape of the latitudinal plots, but showed the most linear trend in the D component as compared to the H or X. There is a bit more scatter in these plots than in others, but overall the general trend from the latitudinal plots is preserved: as distance increases amplitude decreases. This is a strong indication that there is more than just a global signal being registered by the magnetometers. At least in part, what is seen in the signal at Boulder is not the same as what is seen at Honolulu.

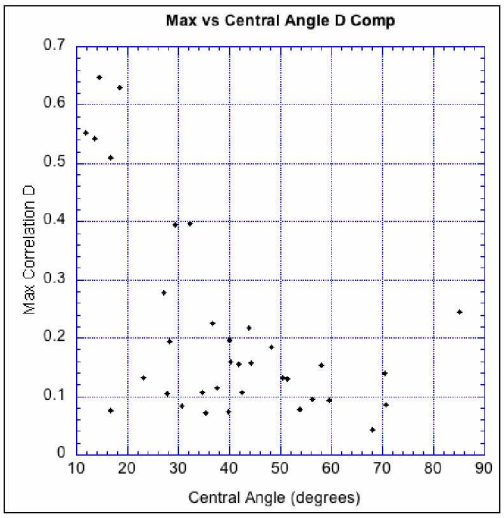

Figure 4.16: Maximum Amplitude vs Central Angle: D Component

For the full width at half maximum analysis, as shown in Figures 4.17, 4.18, and 4.19, recall that the full width of the peak at the half amplitude height can be considered a proxy for the correlation time scale. This means these plots may indicate how long the signals stay correlated. Of particular note for these plots is the presence of periodicities. For a handful of plots, the signals were simply periodic lacking a main peak in the center. These were not excluded from the total analysis. However, the more periodically dominated signals tended to have weaker correlation values.

The width dependence on latitudinal plots presented a surprising result, as demonstrated in Figure 4.17. It was expected that as distance increased the widths would decrease, similar to the trend in the maximum amplitude plots. Contrary to that hypothesis, however, the plots showed a distinct trend that width increased with an increase in distance. This was especially seen in H component, again which aligns with the geomagnetic latitude. The other plots have far more spread but still have a general positive trend in them. This could be a methodological artifact rather than a physical correlation. As the maximum amplitude decreases, the relative position of the half height would also have to go down, increasing the width. This could explain the observed trend, but it is difficult to say with any certainty. If it is true, it could represent that certain scale sizes are lost in the correlation at larger distances, as if the top of the peak, where the smallest correlation size events exist, have been cut off. This supports that theory that there is a local nature to the signals seen in the stations.

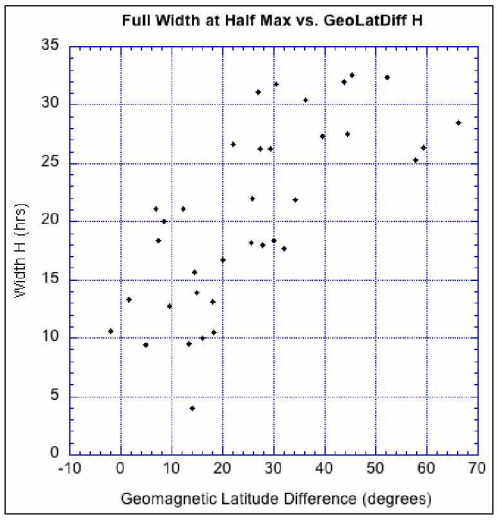

Figure 4.17: Full Width at Half Maximum Amplitude vs Geomagnetic Latitude Difference: H Component

The longitude plots for the full width at half maximum amplitude showed almost no relationship at all. The plots are in general mostly just scatter. The Y and D components show a slight triangular shape, but in general there seems to be little coherence, as shown in Figure 4.18. This could indicate that the correlation time length is independent of longitude for the most part.

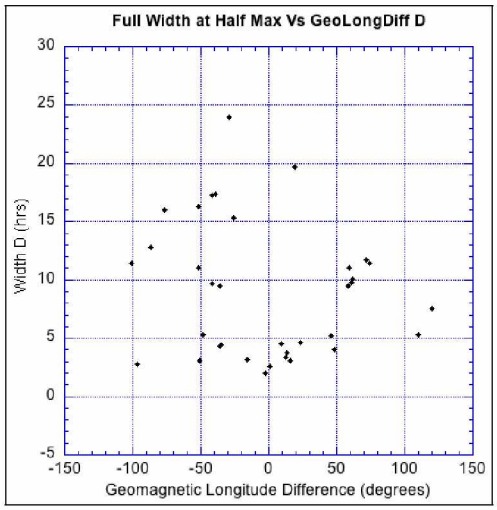

Figure 4.18: Full Width at Half Maximum Amplitude vs Geomagnetic Longitude Difference: D Component

The central angle comparison showed two different trends. The H, X and Z components matched similar trend to Figure 4.17, with a positive relationship between distance and width. The Y and D components have a somewhat triangular pattern, but unlike the longitudinal plots from

the maximum correlation Figure 4.15 and width Figure 4.18, the center is roughly at 45 degrees not centered at zero. This suggests a component dependence linked to the distance measure that is aligned with that component. The Z component's similarities to the H and X could suggest the main strength of the signal is reflected along the HZ plane, frozen to the field lines of the magnetosphere.

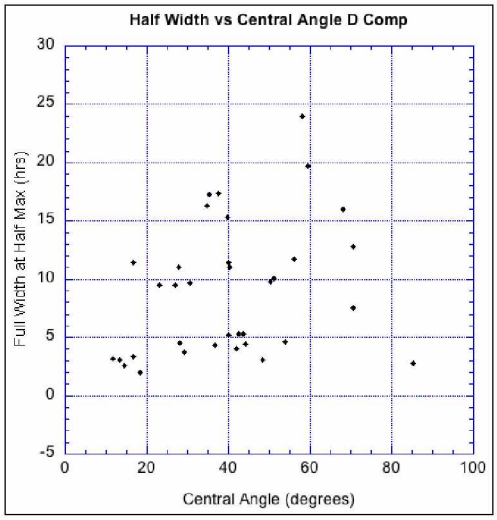

Figure 4.19: Full Width at Half Maximum Amplitude vs Central Angle: D Component

The lead or lag value vs distance plots analysis gave mixed results. A majority of the plots did not have any lead or lag, having the peak centered at zero. As such any interpretation of lead and lag values is focusing on a minority of data set. For the lead/lag vs latitude plots, the H and X plots showed no lead values at all, being completely positive. However, there does not seem to be a noticeable trend otherwise. The Y, D, and Z components all had lead and lag values with an additional feature that after a latitudinal difference of 40 degrees, the spread quickly died away with only a few nonzero values. This could be either an indication that at the point the stations are too far for a lead or lag influence. Another possibility is due to the stations chosen, there was not enough significantly distanced stations for full coverage. Figure 4.20 shows the Z component and the aforementioned change near 40 degrees.

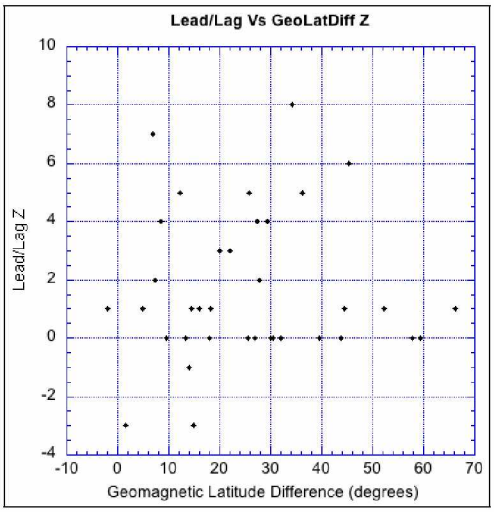

Figure 4.20: Lead/Lag vs Geomagnetic Latitude Difference: Z Component

In the longitudinal case, there is a clear signal in the D and Y components, as shown in Figure 4.21, indicating that the western stations lead the eastern ones. For the stations that do show the presence of a lead or a lag, the larger the distance the stronger the lead or lag appears. Again due to the amount of data points, these results do not share the confidence as compared to the maximum amplitude or full width plots, but the trend is clear. The H and X again show no lead (negative) values. The Z component showed a relatively trendless scatter.

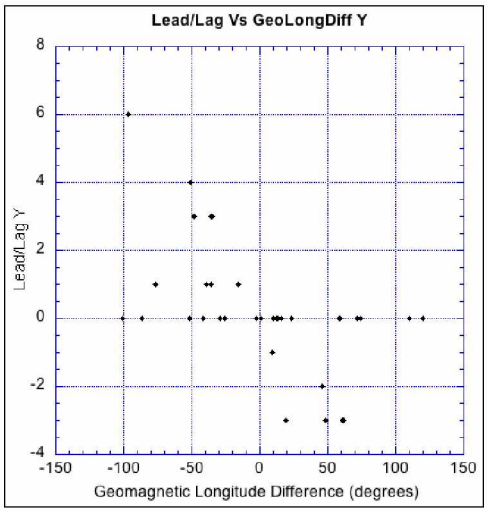

Figure 4.21: Lead/Lag vs Geomagnetic Latitude Difference: Y Component

For the central angle analysis, the H and X components show no real trend besides the presence of only positive values. The Y and D components both show some semi-coherent scatter

without a strongly defined trend. The Z component shows a distinct positive trend as shown in Figure 4.22. This would suggest that as the true distance between stations increases, there is a larger lag between signals in the vertical component.

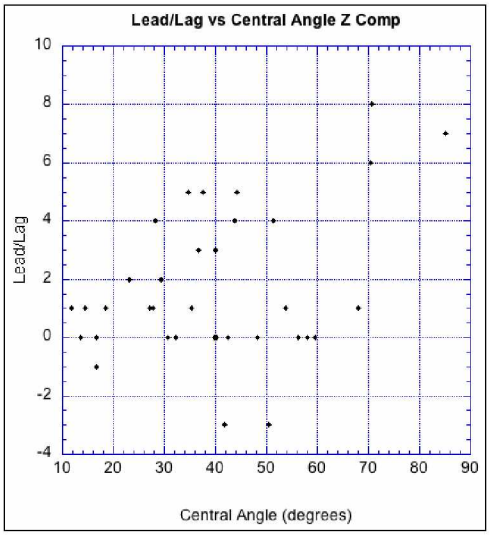

Figure 4.22: Lead/Lag vs Central Angle: Z Component

Cross component cross correlation was performed as a test to see if observed nonlocal correlations were only position based or if there was some connection to waves in the magnetosphere. For the test, both the X and H components of two northern stations, College and Thule, were correlated with both the Z and D components of two equatorial stations, Honolulu and San Juan. If a wave propagates along the magnetic field line but perturbates normal to it, a station in the north could measure it in one of the horizontal components. The Alfvén wave is an example of this. If a wave can both propagate and perturbate normal to the magnetic field line, as the fast mode magnetohydrodynamic wave does, it could register in an equatorial station's Z component. In all cases, the maximum correlation values were weaker than the same component correlations for the same stations, which suggests the latitudinal and longitudinal correlations presented above are the dominant correlation.

4.2 Probability Density Function

The PDF plots across most stations were fairly similar overall. The general pattern was a gentle slope for small bin values with a sudden transition into a steeper drop. At the medium scale sizes, called the mesoscale, a power law is observed with some stations exhibiting a Levy

distribution exemplified by the power law value greater than -2. After the mesoscale region, an even steeper drop is observed until the very end. The final scale sizes usually level out or rebound back up depending on the station. There is some indication that this pattern has variations related to location, but it is not obvious. Discussion of three stations, Boulder, Ottawa, and San Juan follows as case studies of the differences seen from the various stations.

The Boulder plots show the largest power law region of all the plots. Ottawa and Thule show somewhat similar curves in at least one component, yet without a doubt Boulder has the smoothest PDF with the largest power law as shown in Figure 4.23. All components show a mesoscale region with a power law value greater -2 starting around the 0.8 event size. This region extends roughly for an order of magnitude for all but the D component. The D component maintains a steady slope for the majority of the plot, only changing at the very end. This region represents an area of self similarity, where the behavior of signals is roughly scale invariant over that range. As the Sun as been shown to display some self similar behavior [Veltri, 1999], it is possible all the events of these scale size originate from solar activity. It could also be, however, that the signals are magnetospheric in origin.

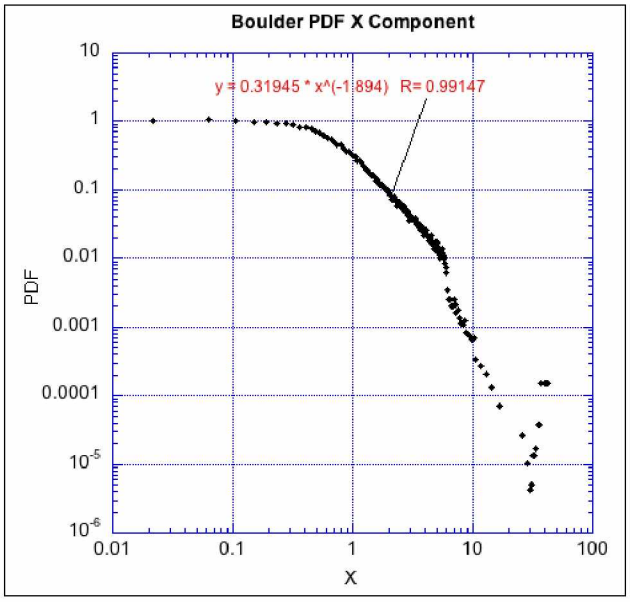

Figure 4.23: Probability Density Function Boulder: X Component

All of the plots exhibit steeper slopes near the normalized scale size 50, then proceed to bounce back. The final few data points could be a binning issue, contamination due to the data

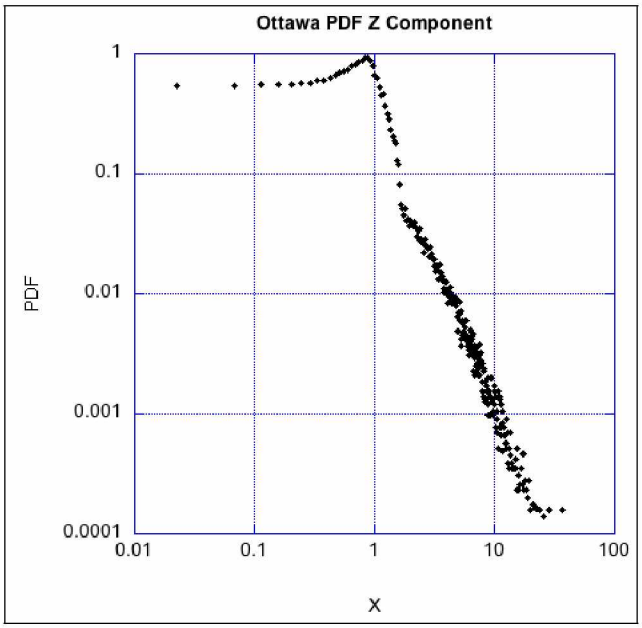

Figure 4.24: Probability Density Function Ottawa: Z Component

cleaning, or could represent an unexpected increase in the probability of large events. If this increased probability was a true signal, it could have a large impact on a risk assessment, as the largest events are often the most damaging and costly. However, it is in the opinion of the researcher that since there is such drastic dissimilarity of the final region compared to the rest of the data, such that the sign of the slope actually switches, those data points are not reliable.

The X, Y, and D components of Ottawa display a similar curve to Boulder, with a more drastic change in slope prior to the mesoscale region. The H and Z components show a sharper transition between regions, with Z showing a positive slope up to the mesoscale region, as depicted in Figure 4.24. This sharper transition and steeper mesoscale region was observed in many of the other stations. All of the plots display a steep region in larger event sizes following the mesoscale region with a curving out at the end for the largest values. While not a 'classic' heavy tail, the end of the plots do show an increased probability compared to a Gaussian normal curve. The faster transition to the steeper power law region indicates a lower risk for large events as compared to Boulder.

All of the San Juan plots display a drastic transition near the 1.2 event size, going from a flat or increasing slope to a steep downward slope. After a short interval, the slope relaxes and the coherence of the line lessens. At the end, as with Ottawa, there is a curving out for the

highest values. This feature is common across most of the stations. There is little difference across components, with D and Y showing positive slopes prior to the main shift compared to the other components, as seen in Figure 4.25. Again the presence of a distinct mesoscale region near a scale size of 1 seems to be a station wide attribute. The steeper slope of the mesoscale region could indicate a lower risk for those events as compared to Boulder or Ottawa. As with the others, the tail values could indicate a larger risk from increased probabilities for the largest scale events.

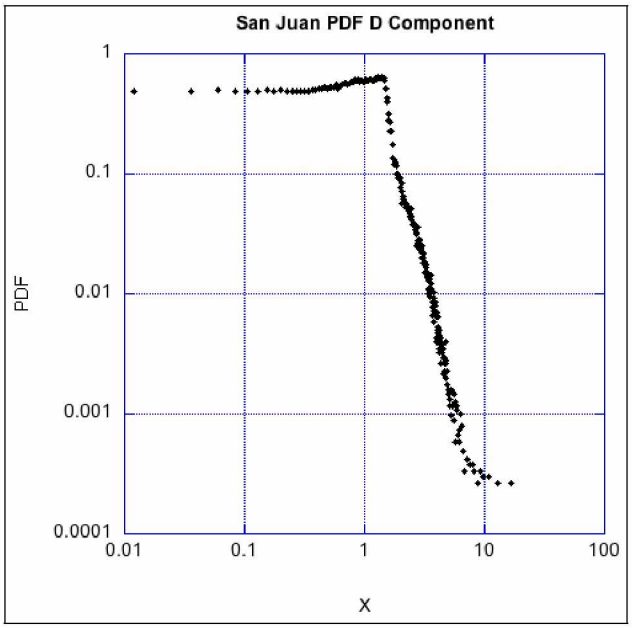

Figure 4.25: Probability Density Function San Juan: D Component

From the PDFs, we see multiple power law regions. The mesoscale region was the most well defined and for some stations had an exponent representing a more Levy distribution. This could suggest self similarity, that is over the range of those scale events the dynamics are scale invariant. The other region of interest, the 'heavy tail', indicates the most impactive events happen more frequently than compared to a Gaussian prediction. The fact there is not a single power law over the full data set suggests that different dynamics are driving different sized magnetic events.

4.3 R/S Statistic

The R/S analysis was performed on all components for all stations. Due to our inability to fully remove all of the periodicities, the plots across all stations were dominated by the periodic signals that were not fully removed by the data preparation. A periodicity can often be identified

in an R/S plot when the data approaching the time value equal to the period of the periodicity has a slope close to one, indicating a strong positive correlation. After passing the period, the slope flattens out to zero, representing a change from correlation to anticorrelation. This behavior can most easily be understood by realizing that the R/S method represents an alternate form of viewing the autocorrelation, where the time values on the x-axis are similar to the time lag between data points in the same signal. For example, for a time lag of 6 weeks, all points that are 6 weeks apart are correlated together, looking to see if there is a pattern. If the change of every point separated by 6 weeks is the same, i.e. all points are increasing over time or decreasing over time in sync with each other, there is a strong correlation. If the data is out of sync, with one side increasing when the other decreases, there is strong anticorrelation. In the case of a periodicity, once the time lag equal to the period has been passed, the points will be out of sync with each other, leading to the observed shift from correlation to anticorrelation. Figure 4.23 shows the behavior near both the annual and diurnal periodicity, where you can see the correlation to anticorrelation switch in both cases. In the case of this data set there are several periodicities, making it very difficult to distinguish what signals are perturbation related and what are affected by the periodic signals. As such, little conclusion beyond the presence of said periodic signals can be drawn about the data.

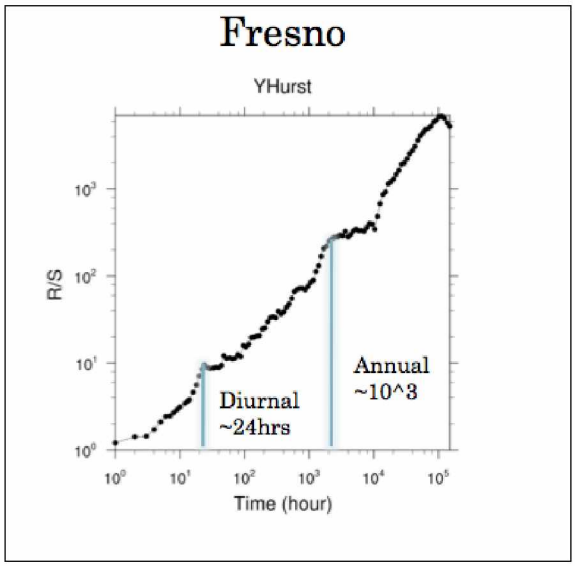

Figure 4.26: R/S Fresno: Y Component

Analyzing the plots for the Fresno Y component, Figure 4.26, and Ottawa F component, Figure 4.27, the various periodicities stand out clearly. First as annotated on the Fresno plot,

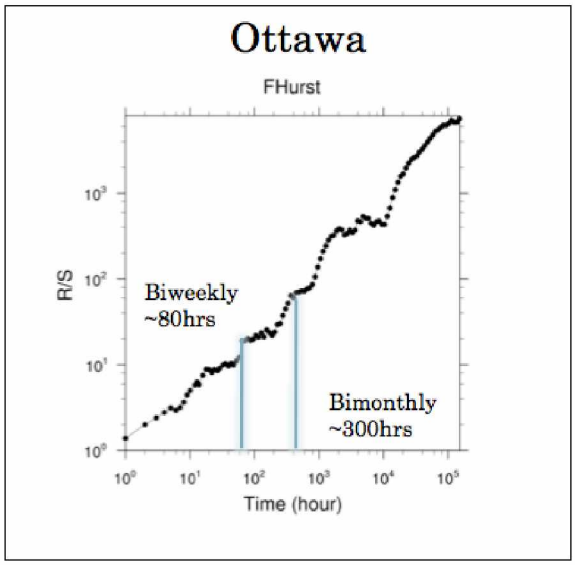

Figure 4.27: R/S Ottawa: F Component

the diurnal periodicity occurs near the 24 hour mark. This was easily identified in all the R/S plots. Occasionally a biweekly period was noted, as shown in the Ottawa plot. Next, a more ambiguous periodicity is observed ranging from 100 to 400 hours, depending on the station. A monthly periodicity was also noted in several stations' plots. Why different stations and components registered this periodicity or set of periodicities differently is unknown. It is possible that there is both a location and component bias related to the various drivers of these signals. As stated in Chapter 2, the nature of these periodicities is thought to be related, at least in part to the magnetic tides, the Sun's rotation, and/or frequency doubling due to the deperiodizer.

The next major periodicity that was apparent in all stations was the annual, occurring around 8,000 hours. In some plots the monthly and annual effect seem to blend together while in others there is a clear distinction between the two. The combination of the two most certainly had the strongest effect on the plots, rendering any analysis on the underlying dynamics in proximity to those time values unreliable.

Finally, for time values following the 10,000 hour mark, there is seen a roughly uniform slope in all plots, though the slope varies between 0.6 and 0.8. This could indicate that the long term time scales of multiple years have some temporal memory. It is difficult to ascertain if this correlation is related to the two periodicities flanking it or if there is an actual perturbation based correlation over that range. Near 100,000 hours there is one last periodicity that occurs, that of the

sun spot cycle which has a 10-14 year period. The presence of all the periodic signals in the R/S made analysis of event based temporal correlation untenable. This is supported by the findings of Montanari, "R/S, the residuals of regression, and the difference variance methods give sizable bias...thus, the use of these methods should be discouraged when the presence of periodicities is suspected" [Montanari et al., 1999].

Chapter 5 Conclusions

This paper examined possible correlations in the ground-based magnetometer network. The analytic methods of Cross Correlation, Probability Density Function, and Hurst R/S gave insight into the spatial and temporal correlations in the system. Through these analyses, a local nature was shown to exist in the signals at each station, indicating that each station experiences some signals unique to that station. Several spatial correlations for both geomagnetic latitude and longitude were also found. Little temporal correlation analysis could be performed due to issues during data preparation. The results presented in this paper are suggestive but not conclusive. The contamination of the data due to periodicities reduces confidence in the validity of the results. The data analysis does suggest a possible nonlinear connection in the magnetometer network which would be worth further investigation.

The methodology for removing the periodicities present in this data set was unsuccessful in cleaning the data to satisfaction. The various periodic signals did not appear to have an exactly constant period, which led to errors in the deperiodizer. The use of Fast Fourier Transform could be utilized at least for the PDF analysis as a comparison to this paper's work as that analysis method is independent of the phase of the data.

From the cross correlation analysis of the magnetic data between the different stations, there are several indications of both latitudinal and longitudinal dependence. The maximum correlation amplitude was strongest for stations in close proximity and fell off quickly as distance increased, especially in the north south alignment. The full width at half maximum amplitude findings showed that smaller scale events were not present in cross correlations between stations far away from each other. This showed an event size dependency on separation distance. From the lead/lag signals, a longitudinal dependence appeared to suggest western stations lead signals observed at the eastern stations. All together, the cross correlation analysis suggests the presence of both local and nonlocal signatures in the signals observed at each station.

The plots of the Probability Density Function (PDF) showed a few regions that appear to be driven by different mechanisms. There is a definite mesoscale region with a power law evident in all stations. The few stations that displayed a power law greater than -2 in this region could be indicating an area of self similarity. This could suggest these events are driven by the solar wind

and eruptive events, as the Sun has displayed some self-similar characteristics. Many stations also depicted a possible signal at the largest event scale. This 'heavy tail' suggests that larger impact events happen with a larger frequency than predicted by a Gaussian curve. These larger events are those of greatest concern for a risk assessment as they often account for the most costly and damaging events. There is some evidence of a latitudinal correlation evident in the variance of where the mesoscale region begins, correlating somewhat to distance from the pole. The presence of different distinct regions, some power law and some not, suggest different dynamics could be driving events at those scale sizes.

The R/S analysis was heavily dominated by the various periodic signals still present in the data. The diurnal, annual, sunspot cycle, as well as a multitude of weekly to monthly signals, tended to mask any other correlations that could have been analyzed. There was some evidence for a temporal correlation at the multiyear time scale, but was difficult to verify. In the future, better removal of the periodicities should allow a better look at the temporal memory of the system. This would lead to to a better understanding about how the system is influenced by past events on different time scales.

Future work would involve the development of an improved deperiodization method. Once a successful method is devised, application of the R/S analysis on the current data set, as mentioned above, could lead to a better understanding of the temporal memory in the system. Expanded data sets, such as India's Alibag Magnetic Observatory's record of over 111 years of magnetic observations would provide a much longer data record than this paper's 18 year record. This could be useful in identifying solar cycle impacts on the data and would have more statistical significance in a complex dynamical system sense. Expansion of the spatial choices of the stations could improve understanding of the impacts of the various periodicities. Correlating the various scale sizes of events to the observed phenomena in the magnetosphere and from the Sun could help understand the dynamics driving the different regions of the PDF. A cost analysis of the space weather impacts would need to be conducted in order to create a risk assessment. The observed local nature of the signals in the magnetometer network could be used to regionalize the risk assessment, so that only data taken from stations in close proximity to the area of interest would be needed, leading to a more accurate picture of that region's vulnerabilities. A risk assessment would present the frequency of different size events coupled with their impacts and costs on a region. As space weather events

adversely affect many of the technologies society relies on such as the power grid and satellite communication, a risk assessment of these potential hazardous and damaging phenomena could lead to improvements in the mitigation and prevention strategies currently in place. This would lead to a safer, more reliable infrastructure better protected from the impacts of space weather on technology and society.

References

Boteler, D., Pirjola, R., and Nevanlinna, H. (1998). The effects of geomagnetic disturbances on electrical systems at the Earth's surface. *Advances in Space Research*, 22(1):17–27.

Cliver, E. (2006). The 1859 space weather event: then and now. *Advances in Space Research*, 38(2):119–129.

Evans, K. (2006). Fluxgate magnetometer explained. Technical report, INVASENS.

Fisher, G. (2003). Integrating space weather and meteorological products for aviation. *Bulletin of the American Meteorological Society*, 84(11):1519–1523.

Fisher, G. et al. (2009). 2009 community review of the ncep space weather prediction center. Technical report, University Corporation for Atmospheric Research.

Gummow, R. and Eng, P. (2002). GIC effects on pipeline corrosion and corrosion control systems. *Journal of Atmospheric and Solar-Terrestrial Physics*, 64(16):1755–1764.

Kerridge, D. (2001). INTERMAGNET: Worldwide near-real-time geomagnetic observatory data. In *Proceedings of the Workshop on Space Weather, ESTEC*, volume 34.

Kivelson, M. G. and Russell, C. T. (1995). *Introduction to space physics*. Cambridge University Press.

Lanzerotti, L. J. (2001). Space weather effects on technologies. *Geophysical Monograph*, 125:11–22.

London, I. C. (2015). How a fluxgate works. http://www3.imperial.ac.uk/pls/portallive/docs/1/20059696.PNG. Accessed: 2015-3-22.

Love, J. J. and Rigler, E. J. (2014). The magnetic tides of Honolulu. *Geophysical Journal International*, 197:1335–1353.

Mandelbrot, B. B. and Wallis, J. R. (1969). Robustness of the rescaled range r/s in the measurement of noncyclic long run statistical dependence. *Water Resources Research*, 5(5):967–988.

Montanari, A., Taqqu, M., and Teverovsky, V. (1999). Estimating long-range dependence in the presence of periodicity: an empirical study. *Mathematical and computer modelling*, 29(10):217–228.

NCAR (2015). Buil-in functions: regline. https://www.ncl.ucar.edu/Document/Functions/Built-in/regline.shtml. Accessed: 2013-3-17.

NSF (2015). Welcome to SHINE. https://www.shinecon.org. Accessed: 2015-4-14.

Parks, G. (2004). *Physics of Space Plasmas*. Westview Press, 2nd edition.

Pirjola, R., Kauristie, K., Lappalainen, H., Viljanen, A., and Pulkkinen, A. (2005). Space weather risk. *Space Weather*, 3(2).

Price, C. and Newman, D. (2001). Using the R/S statistic to analyze AE data. *Journal of Atmospheric and Solar-Terrestrial Physics*, 63(13):1387–1397.

Rasson, J. L. (2007). Observatories, intermagnet. In *Encyclopedia of Geomagnetism and Paleomagnetism*, pages 715–717. Springer.

Reiff, P. (1999). The Sun-Earth Connection. http://space.rice.edu/IMAGE/livefrom/sunearth.html. Accessed: 2013-3-5.

Simpson, S. (2004). A sun-to-mud education in two weeks. *Space Weather*, 2(7).

Space Studies Board et al. (2008). *Severe Space Weather Events–Understanding Societal and Economic Impacts:: A Workshop Report*. National Academies Press.

USGS (2012). U.S. Geological Survey: National Geomagnetism Program - Intstrumentation. http://geomag.usgs.gov/monitoring/instrumentation.php. Accessed: 2014-3-21.

Veltri, P. (1999). MHD turbulence in the solar wind: self-similarity, intermittency and coherent structures. *Plasma Physics and Controlled Fusion*, 41(3A):A787.